Coordination of protein synthesis and decay in mammalian cells

Michael Shoujie Sun[1†], Benjamin Martin[1†], Joanna Dembska[1], Cédric Deluz[1], David M. Suter[1,2*]

[1]Institute of Bioengineering, School of Life Sciences, Ecole Polytechnique Fédérale de Lausanne (EPFL), Lausanne 1015, Switzerland

[†]These authors contributed equally

[2]Lead contact

*Correspondence to: david.suter@epfl.ch

Abstract

Protein synthesis and decay rates must be tightly coordinated to ensure proteome homeostasis. How this coordination is established is unknown. Here we use quantitative live cell imaging combined with computational inference to determine how changes in global protein synthesis rates alter protein decay rates. We identified two modes of adaptation hinging on differential responses of the cell cycle to changes in protein synthesis rates. A passive adaptation of protein degradation and dilution rates operates in cells tightly coupling proliferation rate to protein synthesis rates, allowing to partially buffer changes in proteome concentrations with increased loss of short-lived proteins. In contrast, the proliferation rate of mouse embryonic stem cells (mESCs) is hyposensitive to moderate changes in protein synthesis. mESCs uncouple protein degradation and dilution rates and robustly maintain their protein levels. Our work illuminates the complex interplay between protein synthesis, degradation, and cell division to regulate proteome homeostasis.

Keywords

Protein turnover, protein synthesis, protein degradation, protein dilution, cell proliferation, proteasome, tandem fluorescent timer, passive adaptation, superstatistical modeling, Bayesian inference.

Introduction

Proteins are the central macromolecular components of cellular machineries. The cellular proteome must be constantly turned over to eliminate misfolded or damaged proteins, maintain proteome homeostasis and adapt it to external stimuli. Protein turnover depends on the combined activity of protein synthesis and decay. The rates of these processes need to be adjusted to maintain proteome concentration and stoichiometry within a tight range, which is essential to maintain cellular functions (Neurohr et al. 2019).

Protein synthesis rate depends on mRNA concentration and translation rate, while protein decay depends on degradation and dilution through cell growth and division. The ubiquitin-proteasome system (UPS) and autophagy are responsible for active degradation of proteins and protein complexes. The UPS is responsible for the degradation of most cellular proteins, while autophagy is mainly involved in protein degradation upon cellular stress (Dikic and Elazar 2018). The rates at which proteins are synthesized and degraded can be adjusted to cellular needs to regulate the pace of proteome renewal (Balakrishnan et al. 2022; Seinkmane et al. 2022) for specific cellular functions (Klein, Castillo, and Jordan 2015; Ramachandran et al. 2018; Kristensen, Gsponer, and Foster 2013) or to reach a specific growth or division rate (Honda et al. 2022; Balakrishnan et al. 2022; Liu et al. 2021). The respective contributions of degradation and dilution to protein-specific decay vary broadly depending on the efficiency of their active degradation, i.e. short-lived proteins are mostly decaying by proteasomal degradation, while proteins with half-lives longer than the cell cycle decay mainly by dilution.

Phenotypically identical cells display substantial variability in global protein synthesis and degradation rates (Alber et al. 2018; Basier and Nurse 2024). These rates are correlated at the single-cell level in mouse embryonic stem cells (mESCs), thereby buffering variability in protein levels (Alber et al. 2018). One communication channel between protein synthesis and degradation is the Integrated Stress Response (ISR). In response to the accumulation of unfolded proteins, the ISR induces the segregation of mRNAs into stress granules to inhibit their translation (Pakos-Zebrucka et al. 2016; Arimoto et al. 2008). In contrast, to which extent variations in global protein synthesis rates elicit corresponding changes in protein decay rate is unclear (Zhang et al. 2014; Dai et al. 2013).

Here we use quantitative analysis of protein turnover in live cells combined with a new computational inference scheme and label-free quantification mass spectrometry to dissect how changes in protein degradation and dilution rate adapt to changes in synthesis rate. Our study reveals distinct modes by which cells adapt their protein degradation and dilution rates to change in protein synthesis rates, resulting in variable capacities in maintaining protein levels.

Results

Changes in protein synthesis rates elicit changes in protein decay rates

To monitor protein synthesis and degradation rates in live cells, we used the Mammalian Cell-optimized Fluorescent Timer (MCFT) (Alber et al. 2018), which consists of a translational fusion between the fast-maturing sfGFP and the slow-maturing mOrange2 fluorescent proteins (Fig.1a). Because of these differences in maturation rates, the relative changes in green (sfGFP) and red (mOrange2) fluorescence contain information about changes in synthesis and degradation rates (Alber et al. 2018; Barry et al. 2016; Khmelinskii et al. 2012) (Supplementary Text). We fused the MCFT to a SNAP-tag, which allows orthogonal measurement of degradation rates upon pulse-labeling with a SNAP-tag dye (Alber et al. 2018; Alber and Suter 2018; Bodor et al. 2012). We additionally fused a PEST element to the C-terminus, allowing to directly address the protein to the proteasome (Rechsteiner and Rogers 1996) (Fig.1a) and that results in a high degradation rate (k_{deg}) (Fig.S1a) of the fusion protein (Short-Lived Timer-SNAP or SLT). This allows using the SLT degradation rate as a direct readout of proteasome activity. To infer changes in MCFT synthesis and degradation from fluorescence trajectories, we used a mathematical model (Methods, Supplementary Text) described in (Alber et al. 2018) that we modified to distinguish protein decay by active degradation (k_{deg}) from the decay through dilution occurring upon cell division (k_{dil}) (Fig.1b). From this model, an analytical relationship can be derived at steady-state (Methods, Supplementary Text) between the sfGFP to mOrange2 fluorescence ratio (called G/R hereafter) and the decay rate ($k = k_{dil} + k_{deg}$) of the MCFT (Supplementary Text).

We then aimed at quantifying how protein decay rates (k, denoting hereafter the fold-change in decay rate) adapt to changes in global protein synthesis rates (S, denoting hereafter the fold-change in synthesis rate). Note that S represents changes in global protein production, which itself depends on many parameters such as the availability of the translation machinery, translation efficiency, and the pool of mRNA that is available. We reasoned that the ideal approach should allow global, tunable, fast, and reversible inhibition of global protein synthesis at the level of translation. We thus decided to use cycloheximide (CHX) to block the elongation of polypeptide chains by the ribosome partially. We treated SLT-expressing NIH/3T3 fibroblasts with 56 different concentrations of CHX ranging from 0.002 to 0.5 µg/ml for 48 hours (Fig.1c, Supplementary Table 1). To avoid biases due to altered cell viability, we determined the CHX concentration range at which cells keep proliferating exponentially, which was up to 0.2 µg/ml of CHX (Fig.S1b, Methods). We then performed SNAP pulse-chase labeling followed by live-cell imaging for 12 hours while maintaining the respective CHX concentrations (Fig.1d). We used sfGFP and mOrange2 fluorescence intensities to infer changes in S and k (Methods), and the integrated sfGFP intensity to compute the total MCFT protein amount P. We also orthogonally measured k_{deg} directly by quantifying the SNAP-SiR647 signal decay (Fig.S1c),

and protein dilution rates (k_{dil}) by quantifying changes in cell numbers (Fig.S1d). As expected, *S* decreased with increasing CHX concentrations (Fig.1e). *P* decreased but less strongly than *S* upon CHX treatment (Fig.1f). Both k_{deg}, k_{dil}, and *P* decreased with increasing CHX concentrations (Fig.1g-i), indicating that the protein degradation and cell cycle machineries are sensitive to changes in *S*. Overall, *P* and *k* decreased to a lesser extent than *S*, suggesting that the partial buffering of protein levels is caused by partial adaptation of *k* to changes in *S* (Fig.1i-j). Changes in k_{dil} and k_{deg} scaled linearly with a small offset, indicating that they adapt to changes in *S* in a relatively similar manner (Fig.1k). Results obtained using SNAP pulse-chase labeling yielded congruent results (Fig.S1e). Therefore, our results deviate from a perfect adaptation scenario in which the adaptation of k_{deg} *and* k_{dil} would allow to fully maintain *P* over the whole range of *S*.

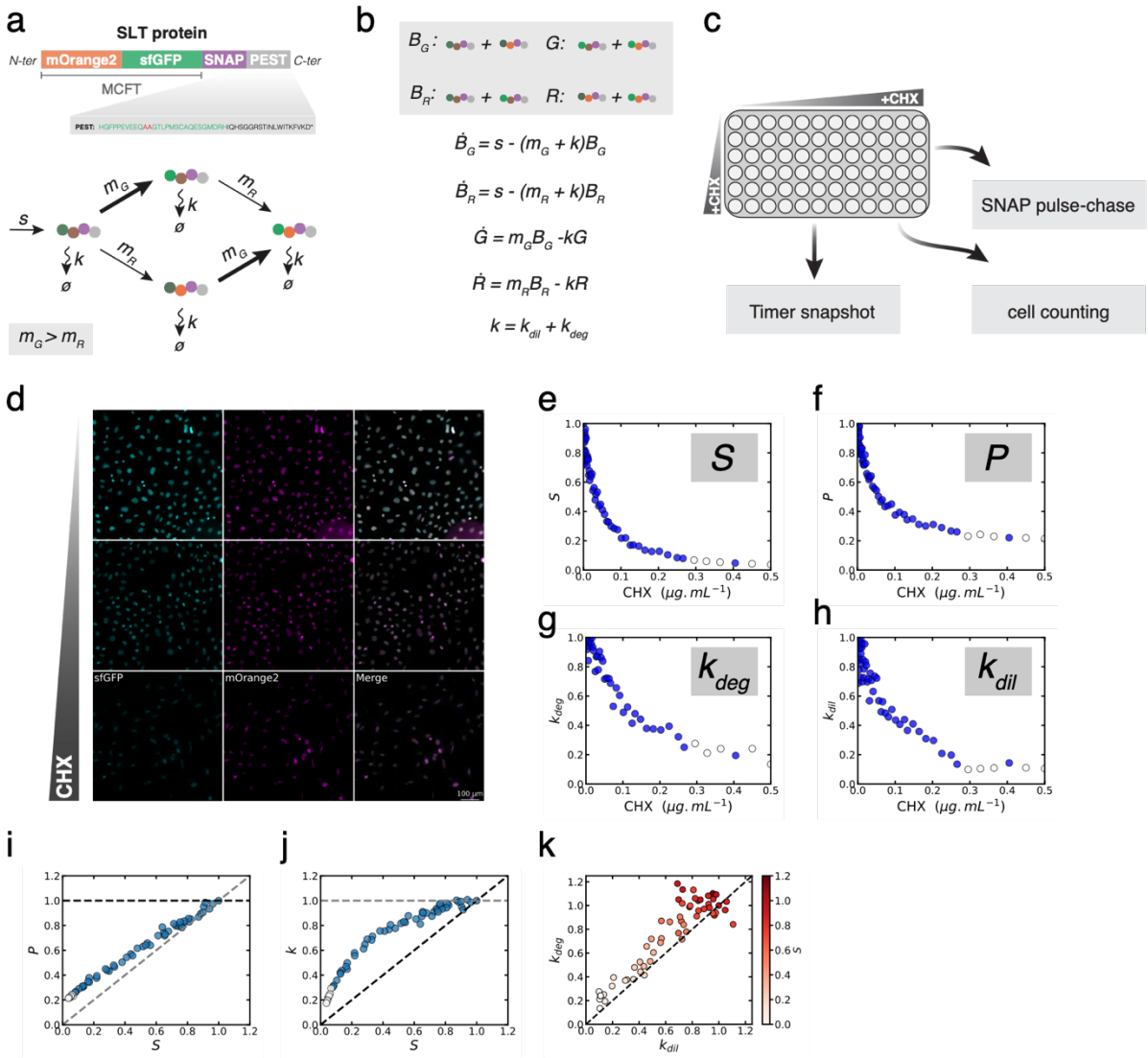

Figure 1: Relationships between *S*, *P*, k_{deg}, and k_{dil} upon CHX treatment. a, Scheme of the short-lived timer (SLT) construct. MCFT: Mammalian Cell-optimized Fluorescent Timer. **b.** Set of ordinary differential equations describing the changes in green and red fluorescence of the

MCFT depending on the protein synthesis (S) and decay (k) rates. m_G and m_R: maturation rates for sfGFP and mOrange2, respectively. B_G: Black green, i.e. sfGFP protein that did not mature yet; B_R: Black red; i.e. mOrange2 protein that did not mature yet. G: green (mature sfGFP); R: red (mature mOrange2). **c,** Experimental design to determine changes in S, k_{deg}, k_{dil} and P after treatment with different CHX concentrations. **d**, Green (cyan) and Red (magenta) fluorescence snapshots of NIH/3T3 cell populations treated with different CHX concentrations (from top to bottom: 0.008, 0.1125, and 0.5 µg/mL) for 48 hours. **e-h,** Fold-change in synthesis rate S (**e**), protein level P of the SLT (**f**), degradation rate k_{deg} (**g**), and dilution rate k_{dil} (**h**), with respect to CHX concentration. **i,** Fold-change in P with respect to S. **j,** Fold-change in k with respect to S. Black dashed lines: prediction for perfect adaptation; Gray dashed lines: prediction for no adaptation. **k,** Fold-change in k_{deg} with respect to the fold-change in k_{dil}. Color bar: fold-change in S. x=y diagonal black dashed line: equal fold-change in degradation and dilution rates. White dots: data points for which exponential division was lost. The values shown for S, P, k, k_{deg} and k_{dil} are normalized on the respective values for control conditions.

A passive adaptation model recapitulates changes in protein decay upon decreased protein synthesis rates

We then asked whether the decreased production of protein degradation and dilution machineries caused by a decrease in S would be sufficient to explain the partial adaptation of k to S in NIH/3T3 cells. Briefly, we modeled three interdependent sets of proteins: the degradation machinery (DeM), the dilution machinery (DiM), and a protein of interest (POI) (Fig.2a). The degradation and dilution machineries are required for their own decay and the decay of the POI. The model assumes that translation inhibition by CHX scales down S of all proteins (DeM, DiM, and POI) by the same factor (Fig.2a). As CHX reduces DeM and DiM synthesis, the protein level of DeM and DiM decreases, subsequently reducing their decay rate. We calculated that after reaching equilibrium, the protein level of DeM and DiM, and thus the POI decay rate will scale as the square root of S (Fig.2a, Supplementary Text), leading to the same scaling for the POI (Fig.2a, Supplementary Text). We used our SLT data to ask how well our model explains changes in the activity of the degradation and dilution machineries. We found the passive adaptation model to provide a good approximation of the relationships of S vs k_{deg} and vs k_{dil} (Fig.2b-c). However, while following the general trend for passive adaptation, k_{deg} stayed stable upon moderate changes in S. This suggests that spare degradation resources allow to maintain k_{deg} upon a modest decrease in S in NIH/3T3 cells. We also found that changes in P upon changes in S could be approximated by the passive adaptation model (Fig.2d). Log-likelihood computation and bootstrapping for model selection (Methods) confirmed these observations (Fig.S2a).

We next asked whether changes in k_{deg} and k_{dil} upon a decrease in S are interdependent. Since the proteasome is a long-lived machinery (Nandi et al. 1997; Khan et al. 2001; Tanaka and Ichihara 1989; Cuervo et al. 1995), we reasoned that its concentration might be more dependent on k_{dil} than k_{deg}. To test this hypothesis, we took advantage of the global gene expression and cell proliferation regulation by the MYC transcription factor (Jha, Kouzine, and Levens 2023) and the availability of a specific MYC inhibitor 10058-F4 (Huang et al. 2006) (MYCi). Since MYC enhances the global transcriptional and translational activity and directly activates cell cycle regulators to stimulate cell proliferation (Jha, Kouzine, and Levens 2023), we reasoned that MYCi would both decrease S and k_{dil} independently. We treated NIH/3T3 cells for 48 hours with 56 doses of MYCi ranging from 0.26 to 64 μM (Fig.2e, Supplementary Table 2). As expected, we observed a MYCi dose-dependent decrease in S (Fig.2f, Fig.S2b) and a strong, close-to-perfect adaptation of k_{dil} to changes in S (Fig.2g and Fig.S2c). In contrast, k_{deg} stayed constant until S went below 50% of its value in control conditions (Fig.2h-i and Fig.S2d). This suggests that a strong decrease in k_{dil} abolishes changes in k_{deg} in response to a decrease in S, and thereby that k_{deg} is strongly dependent on k_{dil}.

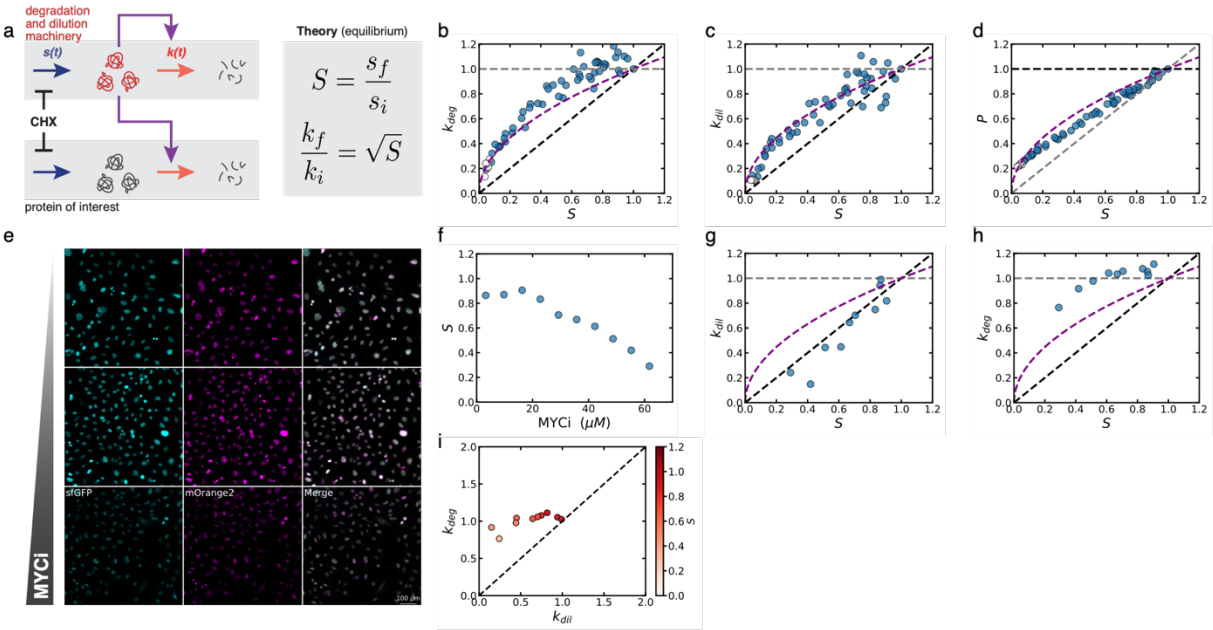

Figure 2: Passive adaptation of *k* and *P* to *S*. a, Chemical scheme of the passive adaptation model and predicted relationship of k and S at equilibrium. Fold-change in k_{deg} (**b**), k_{dil} (**c**), and P (**d**) versus fold-change in S. **e,** Snapshots in green (cyan) and red (magenta) fluorescence for NIH/3T3 cell populations treated with different MYCi concentrations (from top to bottom: 1, 14.4, and 64 μM) for 48 hours. **f,** Fold-change in S with respect to MYCi concentration. Fold-change in k_{dil} (**g**) and k_{deg} (**h**) versus S. Black dashed lines: prediction for perfect adaptation; Gray dashed lines: prediction for no adaptation. Purple dashed curved lines: prediction for passive adaptation. The data are binned in 10 equal bins over the range of MYCi concentrations. **i,** Fold-

change in k_{deg} with respect to the fold-change in k_{dil} upon MYCi treatment. Color bar: fold-change in S for different MYCi concentrations. x=y diagonal black dashed line: equal fold-change in degradation and dilution rates. White dots: data points for which exponential division was lost. The values shown for S, P, k_{deg} and k_{dil} are normalized on the respective values for control conditions.

To test the generality of the passive adaptation model, we generated NIH/3T3 cell lines constitutively expressing the MCFT-SNAP with a mutated, non-functional PEST (long-lived timer or LLT), or fused to three different mouse proteins: NANOG, ESRRB, or SOX2. This resulted in MCFT-labeled proteins characterized by different protein-specific k_{deg} (psk_{deg}) at steady state (Fig.S3a). Given that the LLT has a very low psk_{deg} (Fig. S3a), CHX treatment was extended to 6 days to ensure reaching a steady state. The passive adaptation model recapitulated well the changes in k upon CHX treatment (50 concentrations selected from 0.002 to 0.25 µg/ml at which exponential growth is maintained) for all tested proteins (Fig.3a-d). Interestingly, we found that the protein level change of LLT was closer to perfect adaptation with respect to the other proteins (black dotted line in Fig.3a-d). This can be explained by the low psk_{deg} of the LLT, which thus depends mainly on k_{dil} for its decay (Fig.S3b) and that we found to adapt slightly more than predicted by the passive adaptation model when S reaches < 50% of its original value (Fig.2b-c). To quantify changes of total protein levels, we then labeled all intracellular proteins using N-hydroxysuccinimidyl (NHS) ester that reacts with free amino groups (Neurohr et al. 2019) after treatment with different CHX concentrations. We then quantified changes in the nuclear NHS ester signal in response to a decrease in S after 6 days of CHX treatment (Fig.S3c and Fig.3e). The passive adaptation model explained well the changes in total nuclear protein content at moderate changes in S. When reaching S levels below 50%, changes in total protein levels started to deviate from the passive adaptation model. Similarly to the LLT, this is expected given the long median half-life of proteins in NIH/3T3 cells (47.9 hours, computed from (Schwanhäusser et al. 2011), Supplementary text) that implies a dominant impact of k_{dil} over k_{deg}.

We then asked if passive adaptation could also explain the adaptation of k to S in other mammalian cell types. We generated a knock-in human embryonic stem cell line (hESC) in which the SLT was integrated into the CLYBL locus (Cerbini et al. 2015) (Methods, Fig.S3d-f). Upon treatment with different doses of CHX (Fig.3f), k_{deg} followed the passive adaptation model (Fig.3g) while changes in k_{dil} were closer to perfect adaptation (Fig.3h-i). Changes in P were well-approximated by the passive adaptation model (Fig.3j).

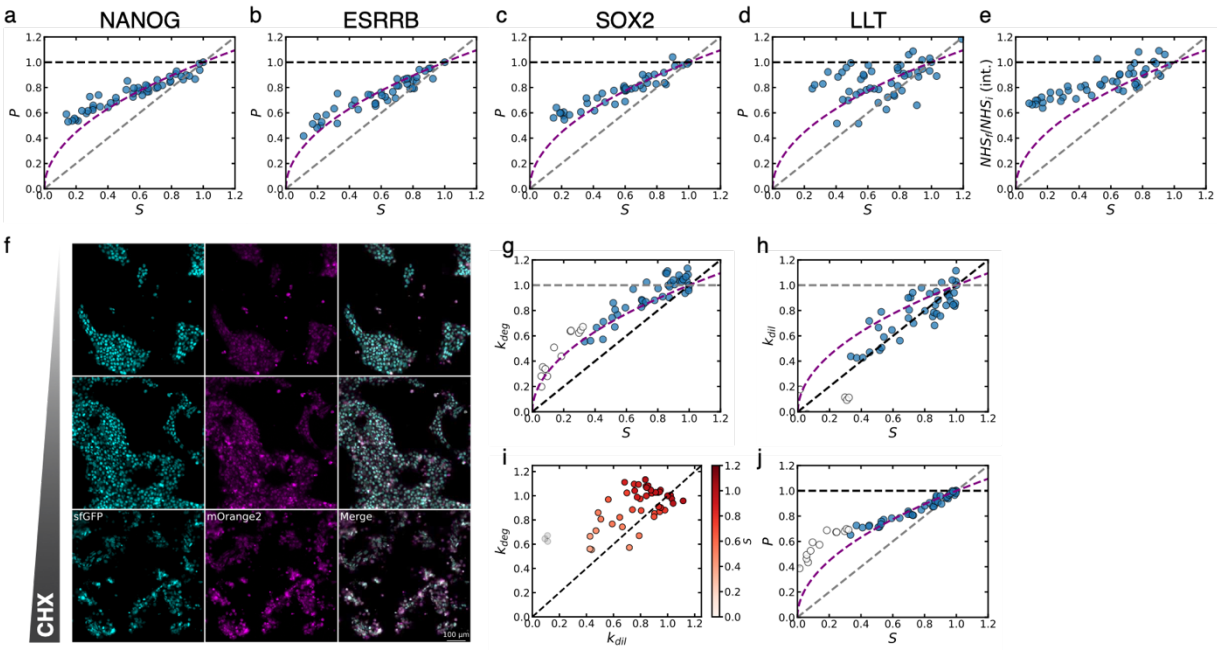

Figure 3: Passive adaptation of *k* and *P* to *S* for other proteins and in hESCs. (a-d), Fold-change of *P* with respect to *S* for NANOG (**a**), ESRRB (**b**), SOX2 (**c**), and the LLT (**d**). **e,** Fold-change in total nuclear protein levels with respect to *S*, measured with NHS-ester. **f**, Green (cyan) and red (magenta) fluorescence snapshots of hESC SLT cell populations treated with different CHX concentrations (from top to bottom: 0.008, 0.1125, and 0.5 µg/mL) for 48 hours. Fold-change in k_{deg} (**g**) and k_{dil} (**h**) vs fold-change in *S* in hESCs. **i.** Fold-change in k_{deg} with respect to the change in k_{dil} in hESCs treated with CHX. Color bar: fold-change in *S* in each condition. **j,** Fold-change in *P* versus *S* for CHX treatment in hESCs. (**a-e, g-h, j**) Black dashed lines: prediction for perfect adaptation; Gray dashed lines: prediction for no adaptation. Purple dashed curved lines: prediction for passive adaptation. White dots: data points for which exponential division was lost. The values shown for *S*, *P*, k_{deg} and k_{dil} are normalized on the respective values for control conditions.

k adapts to changes in *S* within 10-15 hours

We then developed a superstatistical Bayesian approach (Metzner et al. 2015; Mark et al. 2018; Mark, Metzner, and Fabry 2014) to infer time variations of *S* and *k* from MCFT traces (Methods, Supplementary Text, Fig.S4a). To test whether our inference method allows to discriminate dynamic changes in *S* and *k*, we generated synthetic sfGFP and mOrange2 fluorescence trajectories (Fig.S4b-c) using known variations of *S* and *k* (Fig.S4d-e). In all cases tested, our inference approach accurately recovered ground truth time variations of *k* and *S* from the fluorescence trajectories (Fig.S4d-e).

We next used a cell line in which MCFT expression is controlled by a doxycycline (dox)-inducible promoter in NIH/3T3 cells (Alber et al. 2018), allowing to alter the synthesis rate of the MCFT only, without expected changes in its psk_{deg}. We used 28 different step changes in dox

concentrations (Fig.4a) and quantified sfGFP and mOrange2 fluorescence over time (Fig.S4f). In all cases, we correctly inferred expected changes in S and a mostly unaltered k (Fig.4a). Furthermore, data retrodiction (Methods, Supplementary Text) confirmed that our inference accurately reproduces the input data (Fig.S4g). We conclude that our inference scheme allows robust discrimination between changes in S and k from time traces of the MCFT.

We then aimed at quantifying the time scales characterizing the adaptation of k to alterations in S. To do so, we performed time-lapse imaging of the MCFT in NIH/3T3 constitutively expressing the SLT before, during treatment with 0.1 µg/mL of CHX and after CHX washout (Fig.4b, Supplementary Movies 1-2). We then used our inference algorithm to determine changes in S and k from SLT fluorescence time traces. Upon CHX treatment, we observed a sharp decrease in S (Fig.4c) and a progressive decrease in k until reaching a lower plateau (Fig.4d). To quantify the adaptation time delay of k to S, we used a metric (θ) we recently developed that allows quantifying the imbalance between protein influx (governed by S) and outflux (governed by k) (Martin and Suter 2023). Briefly, the imbalance reads $\theta = Pk/S$, such that at equilibrium $\theta = 1$. $\theta > 1$ (respectively $\theta < 1$) indicates an excess of protein outflux (resp. protein influx) with respect to the protein influx (resp. protein outflux) (Martin and Suter 2023). θ reached its steady-state value around 10-15 hours after CHX addition (Fig.4e). Upon CHX release, we observed similar dynamics and delay in the adaptation of k to S and in θ (Fig.4f-h). We performed the same CHX pulse and release experiments in hESCs (Supplementary Movies 3-4), which resulted in a similar delay in the adaptation of k to S (Fig.4i-n). We conclude that passive adaptation of k to changes in S occurs on a time scale of 10-15 hours. Finally, we also performed MYCi pulse and release experiments in NIH-3T3, and we found that S and k reached a steady state within approximately the same time frame as for CHX pulse and release experiments (Fig.S5a-f).

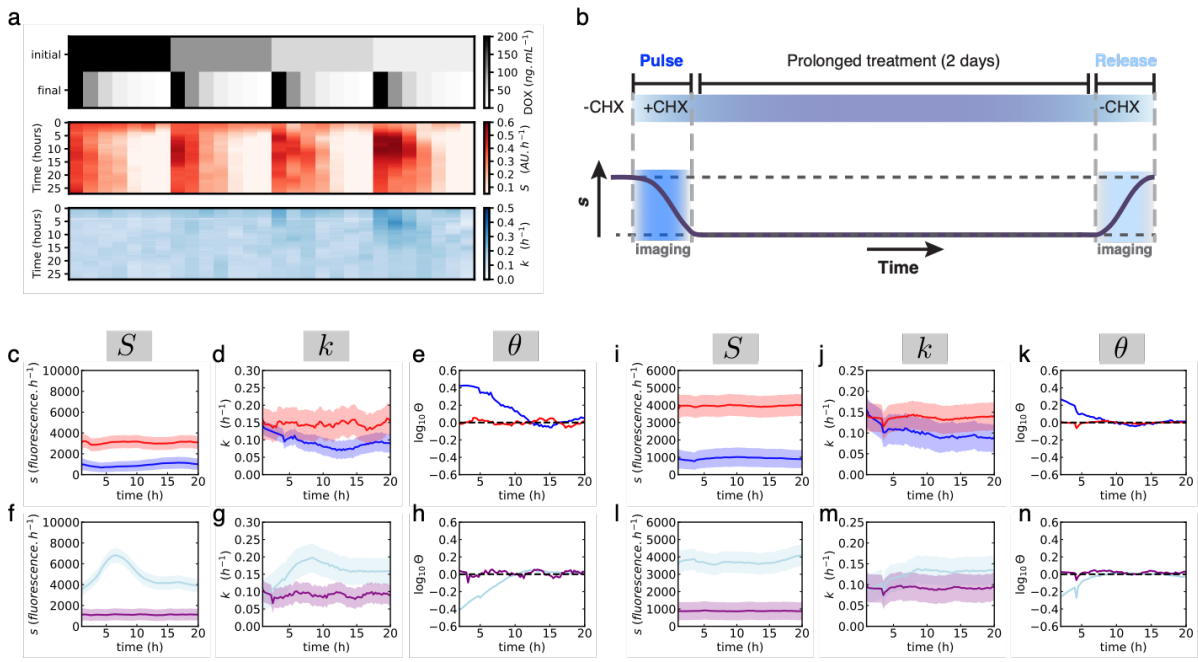

Figure 4: Passive adaptation occurs with a time scale of 10-15 hours. a, Upper panel: dox concentration changes between initial and final concentrations used just before imaging. Heatmaps: temporal variations of *S* (red) and *k* (blue) inferred from SLT trajectories. **b,** Experimental design of CHX pulse and release experiments. (**c-n**) Time-lapse imaging for NIH/3T3 (**c-h**) and hESCs (**i-n**). *S* (**c,i**) and *k* (**d,j**) trajectories inferred from MCFT measurements during CHX pulse. Red: control conditions. Dark blue: CHX pulse. Purple: continuous CHX treatment. Light blue: CHX release. **e,k**, Time variation of the imbalance for the CHX pulse. *S* (**f,l**) and *k* (**g,m**) trajectories inferred from MCFT measurements during CHX release. **h,n,** Time variations of the imbalance for CHX release. (**c-g**) and (**i-m**), plain lines: average of the posterior distribution; shaded regions: SD of the posterior distribution.

Mouse embryonic stem cells display a distinct, biphasic adaptation mode

We next aimed to characterize the adaptation of *k* and *P* to *S* in mouse embryonic stem cells (mESCs). Since mESCs display a modified cell cycle with an altered G1-S checkpoint and inactive Rb protein (Padgett and Santos 2020), we reasoned that their k_{dil} (and consequently k_{deg}), may react differently to changes in *S* as compared to NIH/3T3 and hESCs. We generated an mESC line in which the SLT is knocked into the ROSA26 locus (Methods, Fig.S6a-c) and quantified the response of *k* and *P* to changes in *S* (Fig.5a). In contrast to NIH/3T3 and hESCs, k_{deg} over-adapted to changes in *S* (Fig.5b) and k_{dil} remained high until *S* dropped below ca 60% of its maximal value (Fig.5c-d). Change in *P* vs *S* for the SLT was close to a perfect adaptation (Fig.5e), and this was observed as well for the nuclear proteome (Fig.5f, Fig.S6d). We then performed time-lapse imaging to monitor changes in *k* upon CHX (0.1µg/ml) pulse (Supplementary Movie 5) and release (Supplementary Movie 6). *S* initially dropped upon CHX

addition but rapidly increased thereafter (Fig.5g), suggesting the existence of a mechanism allowing to partially overcome CHX inhibition in the short-term. We also observed decreased *k* values already at the beginning of imaging, suggesting that an active mechanism allows to rapidly shut down protein degradation upon a decrease of *S* (Fig.5h). In a second, slower phase, *S* and *k* adapted to steady-state levels (Fig.5i). Upon CHX release, we observed a rapid increase in *S* that then dropped again, before increasing to *S* levels of control conditions (Fig.5j), while *k* showed a rapid initial increase and reaches steady state towards the end of the imaging period (~20h) (Fig.5k). Protein turnover reached equilibrium after 15-20 hours (Fig.5l). Taken together, our data suggests that mESCs adopt a biphasic adaptation mode in which k_{deg} and *S* respond to CHX within a few hours, but full adaptation occurs in a slower second phase.

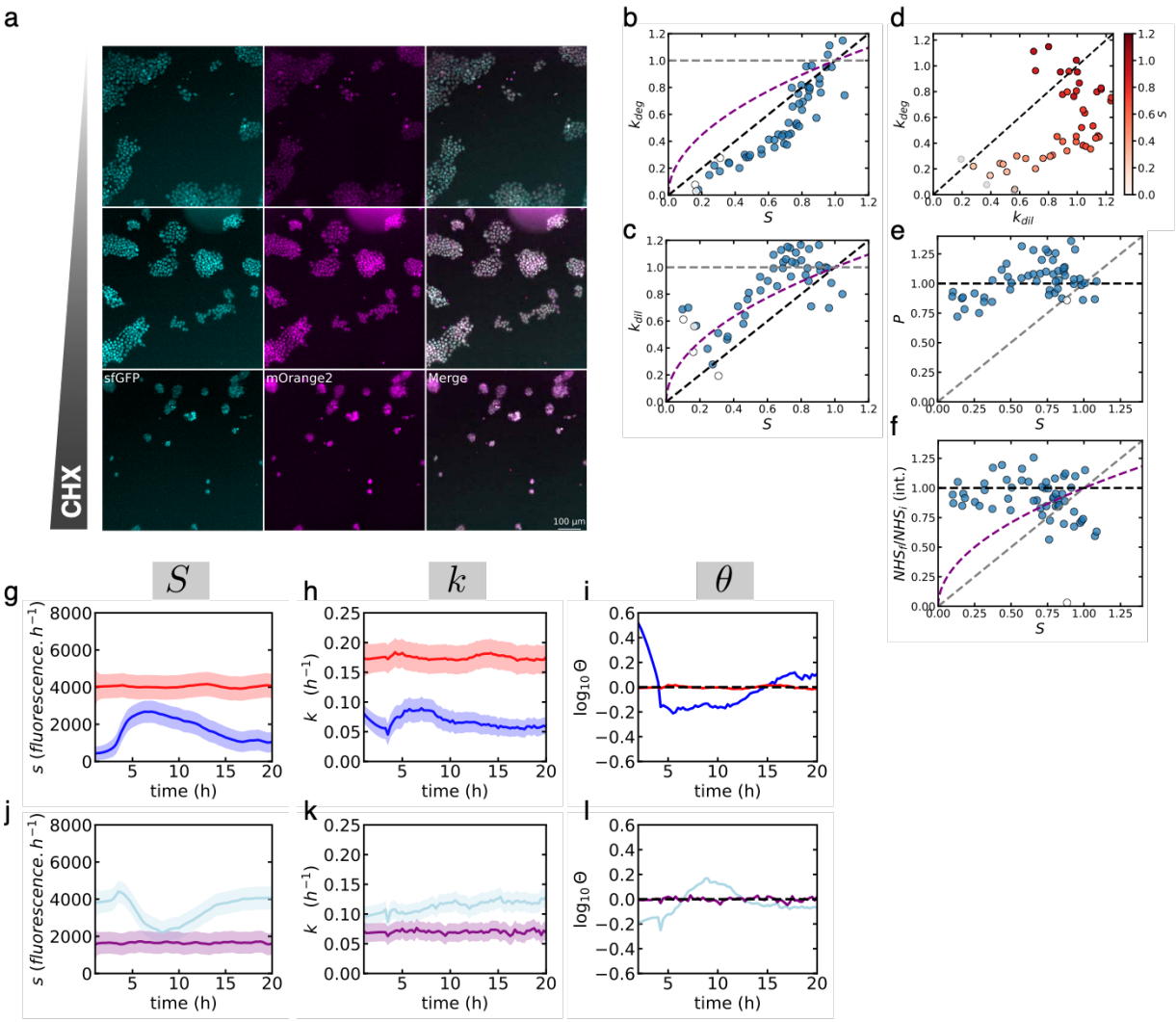

Figure 5: mESC adaptation is inconsistent with a passive mechanism. a, Green (cyan) and red (magenta) fluorescence snapshots of mESC SLT cell populations treated with different CHX concentrations (from top to bottom: 0.008, 0.1125, and 0.5 µg/mL) for 48 hours. Changes in k_{deg} (**b**) and k_{dil} (**c**) vs *S* for CHX treatment in mESCs. **d,** Changes in k_{deg} vs k_{dil} in mESCs treated

with CHX. Color bar: fold-change in *S*. **e,** Changes in *P* vs *S* for the SLT. **f.** Fold-change in total nuclear *P* with respect to *S*, measured with NHS-ester. (**b,c,e,f**) Black dashed lines: prediction for perfect adaptation; Gray dashed lines: prediction for no adaptation. Purple dashed curved lines: prediction for passive adaptation. **(b-f),** The values shown for *S*, *P*, k_{deg} and k_{dil} are normalized on the respective values for control conditions. **g,h**, *S* **(g)** and *k* **(h)** trajectories inferred from MCFT measurements during CHX pulse. **i**, Time variation of the imbalance for CHX pulse. **j,k**, *S* **(j)** and *k* **(k)** trajectories inferred from MCFT measurement during CHX release. **l**, Time variation of the imbalance for CHX release. Red: control conditions. Dark blue: CHX pulse. Purple: continuous CHX treatment. Light blue: CHX release. For **g,h,j,k**, the average (plain line) and the SD (shaded region) of the posterior distribution are represented for each timepoint.

Physiological variability in protein turnover recapitulates cell type-specific adaptation

We next asked whether adaptation of *k* to *S* upon CHX treatment could also explain the relationship between *S*, *k,* and *P* in unperturbed conditions. To do so, we used time-lapse imaging data acquired in the absence of perturbation in i) 5 NIH/3T3 cell lines expressing the SLT, LLT, and the MCFT fused to NANOG, ESRRB, and SOX2, respectively; ii) 40 mESC lines in which the MCFT is internally fused to 40 different endogenously expressed proteins (Alber et al. 2018). We have previously shown that the majority of these 40 proteins exhibit only minor fluctuations in *S*, *k*, and [*P*] over the cell cycle in single cells (Alber et al. 2018). This quasi-steady state allows us to compute *k* for single cells as before for population averages (Methods). Similarly, we computed $S_{conc.}$ and [*P*] for single cells. Note that $S_{conc.}$ is a per-cell protein synthesis rate in concentration per hour unit (Methods). Since $S_{conc.}$ does not correlate with nucleus size (Fig.S7), it can be considered a proxy of single-cell protein synthesis rate, *S* being proportional to its population average. We then normalized the data from all proteins to their median value for S_{conc}, *k,* and [*P*], and aggregated all data points. In NIH/3T3 cells, the correlations of *k* and [*P*] with S_{conc} followed the passive adaptation model, with the exception of very high S_{conc} levels for which few datapoints were available (Fig.6a-b). In contrast, in mESCs the correlation between S_{conc} vs *k* and [*P*] was closer to a perfect adaptation (Fig.6c-d). Altogether, our data indicates that mESCs adapt *k* to S_{conc} more robustly than NIH/3T3 cells, both in the presence or absence of perturbation in *S*.

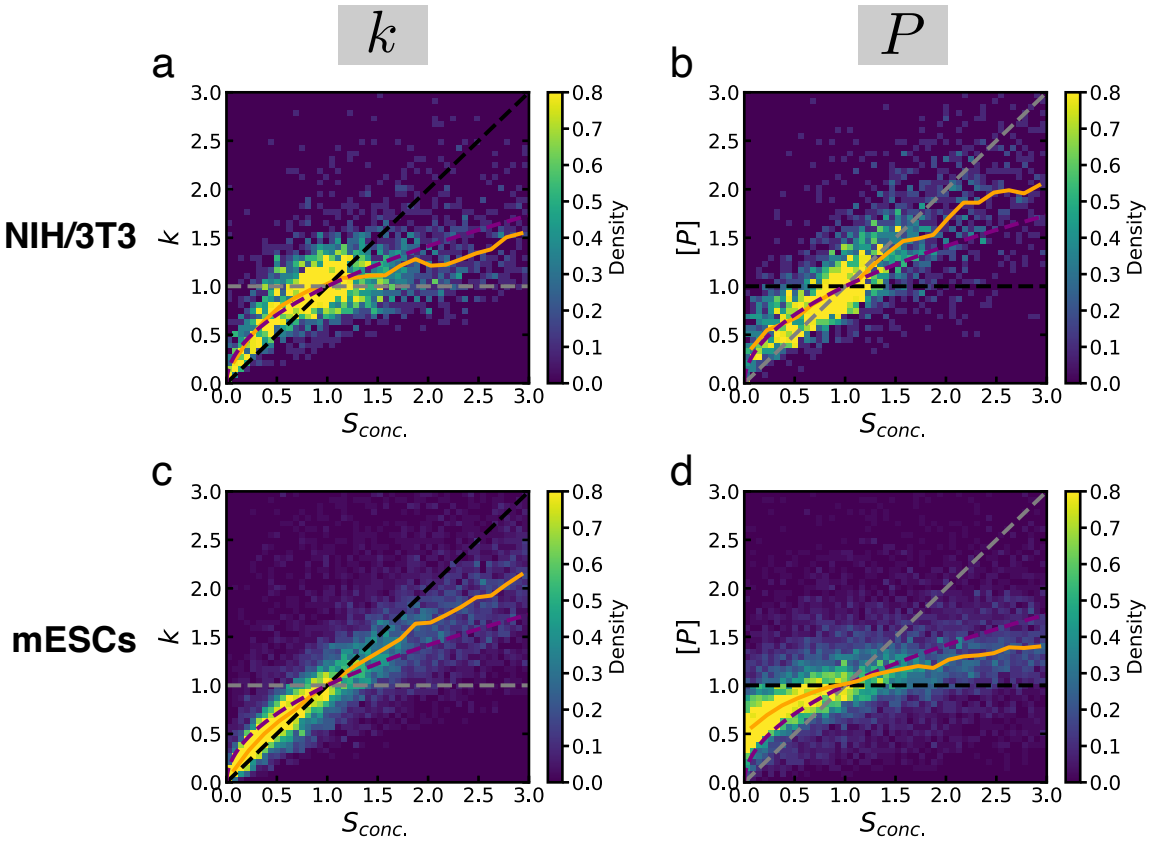

Figure 6: Adaptation of *k* and [*P*] *to* S_{conc} in unperturbed conditions. a,b, *k* versus S_{conc} (**a**) and [*P*] (**b**) in NIH/3T3 cells. **c,d,** *k* versus S_{conc} (**c**) and *P* (**d**) in mESCs. 2D histograms for aggregated and normalized data for 5 (NIH/3T3) or 40 (mESCs) cell lines are shown. Black dashed lines: prediction for perfect adaptation; Gray dashed lines: prediction for no adaptation. Purple dashed curved lines: prediction for passive adaptation. Orange plain line: binned median of the aggregated data.

The proteome of NIH/3T3 cells adapts in a psk_{deg}-dependent manner to a decrease in *S*

We next aimed to quantify the proteome-wide impact of a decrease of *S* in NIH/3T3 cells as a function of the psk_{deg} of different proteins (Schwanhäusser et al. 2011). We cultured NIH/3T3 cells for 4 days with or without 0.1 µg/ml of CHX, which decreases *S* by ca. 3-fold (Fig.4c). We then extracted proteins and performed label-free quantification mass spectrometry to quantify protein-specific alterations of the proteome (Methods). We identified 3788 proteins, of which about 10% and 2.5% were significantly downregulated and upregulated, respectively (Fig.7a-b). We reasoned that we could take advantage of proteome-wide k_{deg} measurements in NIH/3T3 cells (Schwanhäusser et al. 2011) to determine how proteins with different contributions of k_{deg} to *k* maintain their levels upon a decrease of *S*. We first computationally predicted the expected changes in total levels of specific proteins as a function of their psk_{deg}, using the relationship between *S*, k_{deg}, and k_{dil} that we experimentally determined in NIH/3T3, as well as our NHS-

ester measurements to account for the global decrease in total protein levels (Supplementary Text). Since k_{dil} adapted slightly better than k_{deg} in NIH/3T3, the model predicts that proteins with a high psk_{deg} would be lost more than those with a low psk_{deg} upon a decrease in S (Fig.7c). We then classified proteins detected by mass spectrometry in bins of low, medium and high psk_{deg}, and determined their absolute fold-change by factoring-in NHS-ester measurements. As expected from our model, proteins with high psk_{deg} were significantly less preserved than the rest of the proteome (Fig.7d).

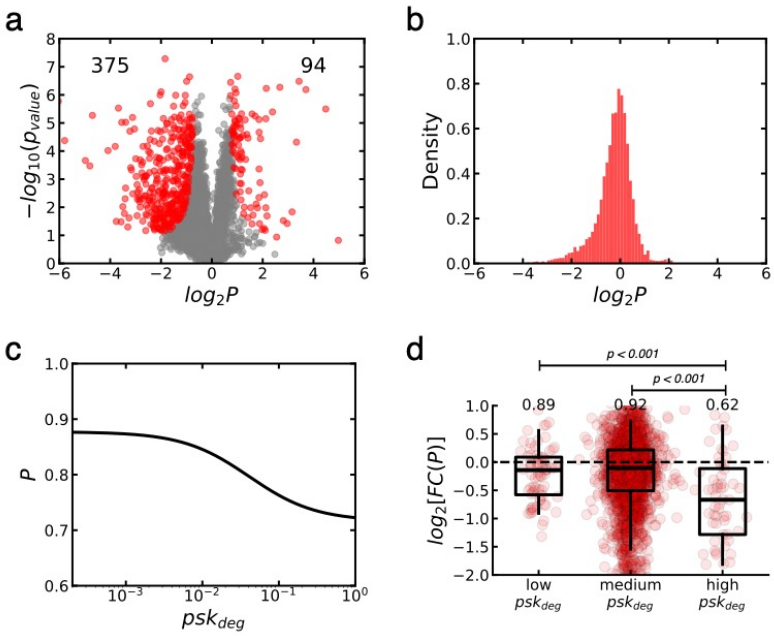

Figure 7: Impact of a decrease in *S* on the proteome of NIH/3T3 cells. a,b, Label-free proteome quantification for cells treated with CHX. **a,** The average of four replicates is plotted for all identified proteins. Red dots: proteins with significant (FDR = 0.01) fold-change in their levels between CHX and control conditions. Each point is the average over quadruplicates of the protein-specific level fold-change. **b,** Distribution of protein level fold-changes between CHX and control conditions. **c,** Predictions of the dependence of the protein level fold-change on psk_{deg}. **d,** Measured protein level fold-change between CHX and control conditions binned according to psk_{deg}. Low psk_{deg}: log10(k_{deg}) < -2.75 h^{-1}; medium psk_{deg}: -2.75 h^{-1}< log10(k_{deg}) < -1 h^{-1}; high psk_{deg}: log10(k_{deg}) > -1 h^{-1}. p values were computed using a two-sided Welch's t-test.

Discussion

Protein turnover rates vary broadly between tissues, cell types, and over time in individual cells (Basier and Nurse 2024; Alber et al. 2018). Variations in these rates directly imply that proteome homeostasis can only be maintained if protein synthesis and decay are quantitatively coordinated. How this coordination is established had remained unknown so far.

To answer this question, we use an approach that uniquely allows to continuously monitor protein synthesis, degradation, and dilution rates in single living cells. While we were able to capture changes in protein synthesis and decay rates over at least one order of magnitude, the MCFT is inherently limited by the boundaries set by the maturation rates of sfGFP and mOrange2. This prevents us from quantifying k_{deg} that are much lower than mOrange2 maturation rates.

We describe two different modes by which dividing cells adapt protein decay to changes in protein synthesis rates. The passive adaptation mode depends on structural relationships between protein synthesis, the cell cycle, and the protein degradation machinery. This mechanism hinges on the sensitivity of cellular proliferation rate to a decrease in protein synthesis rate, which was shown to increase the duration of all cell cycle phases in rat fibroblasts (Okuda and Kimura 1988). The proliferation rate sets the protein dilution rate, which then impacts the turnover of the degradation machinery, which is particularly long-lived (Nandi et al. 1997; Khan et al. 2001; Tanaka and Ichihara 1989; Cuervo et al. 1995) and is thus expected to mainly decay by dilution. While passive adaptation allows only for partial maintenance of overall protein levels, the roughly similar adaptation of k_{deg} and k_{dil} ensures that proteins decaying predominantly by dilution or degradation are affected similarly. This allows passive adaptation to limit changes in proteome stoichiometry to very short-lived proteins, which were lost preferentially due to the slightly less efficient adaptation of k_{deg} as compared to k_{dil}.

In contrast to NIH/3T3 and hESCs, the proliferation rate of mESCs was poorly responsive to a moderate decrease in protein synthesis rates. mESCs have an altered G1-S checkpoint with hyperphosphorylated and thus inactive Rb (Padgett and Santos 2020). When active, Rb normally prevents cells from transiting from G1 to S and needs to be diluted out by cell growth during G1 phase to allow cells to transit toward S-phase (Zatulovskiy et al. 2020). Therefore, the inactivity of Rb in mESCs may at least partially explain the insensitivity of their proliferation rate to mild changes in protein synthesis rates. Furthermore, the maintenance of proliferation rate with substantially decreased synthesis rates likely leads to an increased loss of very long-lived protein complexes such as proteasomes, thus fostering a strong decrease in protein degradation rates. Interestingly, mESCs also displayed a strong acute response to CHX for their protein synthesis and degradation rates. This may ensure that mESCs keep the ability to accumulate proteins at a sufficient pace to progress through the cell cycle when challenged with an acute decrease in translational resources.

In summary, we propose passive adaptation as a structural mechanism by which protein synthesis rates regulate protein decay rates. Our data suggests that cell cycle coupling with protein synthesis rates is an important factor in determining the adaptation of protein decay to altered protein synthesis. Importantly, our study is limited to three cell types and can therefore not broadly predict the adaptation mode of other cellular systems. The mode by which non-dividing cells adapt their degradation rate remains unknown. Finally, while our study shows evidence for a structural, passive adaptation mechanism operating in two different cell types, the mechanistic basis of the active adaptation we uncovered in mESCs remains to be clarified and will be an important open question in the field.

Acknowledgments

This work was supported by EPFL core funding and the Synapsis Foundation Switzerland. The authors want to thank Almut Eisele, Felix Naef, and Maike Hansen for their careful reading of the manuscript and their comments. Fluorescence-activated cell sorting was performed at the EPFL Flow Cytometry Core Facility (EPFL-FCCF). Microscopy and image analysis were performed using the resources of the EPFL Bioimaging and Optics Core Facility (EPFL-BIOP). Mass spectrometry was performed at the Proteomics Core Facility (EPFL-PCF). We particularly thank Maria Pavlou for her expertise in mass spectrometry.

Author contributions

Conceptualization, MS, BM, DS; Methodology, MS, BM, DS; Software, BM; Validation, BM, JD, CD; Formal Analysis, MS, BM; Investigation, MS, BM, JD, CD; Data Curation, MS, BM; Writing — Original Draft, MS, BM, DS; Writing — Review & Editing, BM, JD, DS; Visualization, BM; Supervision, DS; Funding Acquisition, DS.

Declaration of interests: The authors declare no competing interests.

Contact for reagents and resource sharing

Further information and requests for resource sharing and reagents should be directed to and will be fulfilled by the Lead Contact, David Suter (david.suter@epfl.ch).

Data and Code availability

All original codes for reproducing analyses of this paper have been deposited on GitHub and are publicly available. Namely, key scripts for data analysis — inference algorithm and cell segmentation/fluorescence quantification — have been deposited on GitHub: https://github.com/UPSUTER/ProTuCo. Proteomics data will be made available on PRIDE upon publication. Imaging data or other data reported in this paper are available from the lead contact

upon request. Any additional information required to reanalyze the data reported in this paper is available from the lead contact upon request.

Material and methods

Experimental Model and Subject Details

Cell Culture

NIH/3T3 and HEK293T cells were routinely cultured in DMEM (Gibco, 41966029), supplemented with 10% fetal bovine serum (Gibco, 10270-106), 1% penicillin/streptomycin (BioConcept, 401F00H) at 37°C, 5% CO_2. Cells were passaged by trypsinization (Sigma, T4049-100ML) every 2-3 days and maintained at a confluency < 80%.

E14 and CGR8 mouse embryonic stem cell lines were routinely cultured in GMEM (Sigma-Aldrich, G5154) supplemented with 10% ES cell-qualified fetal bovine serum (Gibco, 16141–079), 2 mM sodium pyruvate (Sigma-Aldrich, 113-24-6), 1% non-essential amino acids (Gibco, 11140–050), 1% penicillin/streptomycin (BioConcept, 4-01F00H), 2 mM L-glutamine (Gibco, 25030–024), 100 µM 2-mercaptoethanol (Sigma-Aldrich, 63689), leukaemia inhibitory factor (LIF — in-house), 3 µM GSK-3 Inhibitor XVI (Merck, 361559) and 0.8 µM PD184352 (Sigma-Aldrich, PZ0181), called hereafter 2i, at 37°C, 5% CO_2. Cells were plated on dishes coated with gelatin (Sigma-Aldrich, G9391). Cells were passaged every 2-3 days by trypsinization (Sigma-Aldrich, T4049) when density reached approximately 3.0×10^4 cells/cm^2 (Mulas et al. 2019).

H1 human embryonic stem cells (WiCell, WA01) were routinely cultured as colonies in mTeSR Plus (STEMCELL Technologies, 100-0276) with 0.2% penicillin/streptomycin (BioConcept, 401F00H) at 37°C, 5% CO_2. Cells were plated on dishes coated with Corning Matrigel hESC-qualified matrix (Corning, 354277). Cells were passaged every 4-7 days using the enzyme-free passaging reagent ReLeSR (STEMCELL Technologies, 05872) which preserves colonies, when most of the colonies were large with a dense center. For experiments requiring single cell dissociation, i.e. nucleofection, sorting, imaging, hESCs were passaged using Accutase (Innovative Cell Technology, AT104).

Method Details

Production of lentiviral vectors and generation of stable cell lines

HEK293T cells were seeded at a density of 45,000 cells/cm^2 and transfected using calcium phosphate one day after seeding. Cells were co-transfected with PAX2 (envelope), MD2G (packaging), and the lentiviral construct of interest, and concentrated 120-fold by ultracentrifugation as described previously (Suter et al. 2006). Target NIH/3T3 cells were

seeded at a density of 13,000/cm^2 in a 24-well plate and transduced with 50 µL of concentrated lentivirus. For all dox-inducible cell lines, cells were first transduced with the pLV-pGK-rtTA3G-IRES-Bsd construct (Deluz et al. 2016), selected using 8 µg/mL of blasticidin (Thermofisher, A11139-03), transduced with the pLVTRE3G-construct of interest, and selected with puromycin (Thermofisher, A11138-03) at 2 µg/mL.

Generation of the mESC SLT knock-in cell line

The SLT construct under the control of the EF1α promoter was first inserted using InFusion cloning (Takara) into the pDONOR MCS Rosa26 plasmid (Addgene #37200) containing Rosa26 homology harms. CGR8 cells were co-transfected with pDONOR-SLT, pCMV-RosaL6 ELD (Addgene #37198), and pCMV-RosaR4 KKR (Addgene #37199) with the lipofectamine 3000 transfection reagent (Invitrogen, L3000001) in a 6 well-plate following supplier instructions. These plasmids were a gift from Charles Gersbach (Perez-Pinera et al. 2012). Cells were then maintained for 2 weeks in culture. Cells were afterward sorted as single cells in 96-well plates for bright sfGFP and mOrange2 signals using a FACSAria (BD Biosciences) cell sorter. Around 1% of cells were positive. After 10 days of culture, single colonies were visually checked for MCFT fluorescence signal and the brightest colonies were picked and amplified. 6 clones were then selected for characterization: gDNA was extracted using the DirectPCR Lysis Reagent (Viagen, 301-C) and PCRs were performed to verify the correct integration site of the transgene (Kasparek et al. 2014) (Supplementary Table 3). After gel validation, the bands were cut, the DNA amplicons were extracted with QIAquick Gel Extraction Kit (QIAgene, 28704) and sent to Sanger sequencing (Microsynth) to check the integration site for the presence of indels.

Generation of the hESC SLT knock-in cell line

The SLT construct was inserted using InFusion cloning (Takara) into the pC13N-dCas9-BFP-KRAB plasmid (Addgene, #127968), containing CLYBL homology arms and a CAG promoter. hESCs were co-transfected with pZT-C13-L1 (Addgene, #62196) and pZT-C13-R1 (Addgene, #62197) by nucleofection using the 4D-Nucleofector X Unit (Lonza) and Amaxa P3 Primary Cell kit L (Lonza, V4XP-3012), program CB-150. hESCs were supplemented with 1x CloneR2 (STEMCELL Technologies, 100-0691) supplement for the first two days. These plasmids were a gift from Jizhong Zou (Cerbini et al. 2015). Cells were then maintained for 2 weeks in culture. Cells were afterward sorted as single cells in 96-well plates for bright sfGFP and mOrange2 signals using a FACS Aria (BD Biosciences) cell sorter. Around 0.4% of cells were positive. Cells were supplemented with 1x CloneR2 supplement for the first 4 days, with medium change every other day. After 14 days of culture, single colonies were visually checked for SLT signal and the brightest colonies were picked and amplified. 3 clones were then selected for characterization: gDNA was extracted using the DNEasy Blood & Tissue kit (Qiagene, 69504)

and PCRs were performed to verify the correct integration site of the transgene (Supplementary Table 3). After running PCR products on an agarose gel, the bands were cut, the DNA amplicons were extracted using QIAquick Gel Extraction Kit (Qiagene, 28704) and verified by Sanger sequencing (Microsynth).

Snapshot imaging of the MCFT upon CHX/MYCi steady-state treatments

3 days before imaging, NIH/3T3 cells were seeded on a 96-well plate coated with fibronectin (Sigma, F4759) at a density that does not exceed 80% confluency for each well when imaging starts. After seeding, cells were cultured overnight without CHX in FluoroBrite™ DMEM medium (Gibco, A1896701) supplemented with 10% fetal bovine serum (Gibco, 10270-106), 2 mM L-glutamine (Gibco, 25030–024), and 1% penicillin/streptomycin (BioConcept, 401F00H). The next day, CHX treatment was applied to each well following the designed concentration gradients (Supplementary Table 1). The CHX concentration gradient was made of 56 different concentrations ranging from 0.002 to 0.5 µg/mL. The medium containing the respective CHX concentrations was changed once after 24 hours. After 2 days of treatment, snapshot imaging was performed with Operetta CLS (Perkin Elmer), 20× objectives (Air immersion, Plan Apochromat, NA 0.8), at 37 °C, 5% CO_2. For the sfGFP channel, the following filters were used: Ex: BP 435-460, 460-490, Em: HC 500-550. For the mOrange2 channel, the following filters were used: Ex: BP 490-515, 530-560, Em: HC 570-650.

Experiments with H1 hESCs and CGR8 mESCs were performed similarly, except for culture conditions. hESCs were cultured in mTeSR1 without phenol red (STEMCELL Technologies, 05876) and seeded on a 96-well plate coated with Corning Matrigel hESC-qualified matrix (Corning, 354277). A 10 µM ROCK Inhibitor (Y-27632) (MilliporeSigma, SCM075) was added at the time of seeding. mESCs were cultured in phenol-red free N2B27 + 2i/LIF medium and seeded on a 96-well plate coated with laminin 511 (BioLamina, LN511-0202). Before starting CHX treatment, mESCs were cultured for at least 2 weeks in N2B27 + 2i/LIF medium.

A similar protocol was used for MYCi treatment. The MYCi concentration gradient was made of 56 different concentrations ranging from 0.26 to 64 µM (Supplementary Table 2).

Live imaging of the MCFT upon CHX treatment/release

3 days before imaging, NIH/3T3 cells were seeded on a 96-well plate coated with fibronectin (Sigma, F4759) at a density that does not exceed 80% confluency for each well when imaging starts. Four conditions were designed: control (-CHX), CHX (2 days treatment with 0.1 µg/ml CHX before imaging), pulse (0.1 µg/ml CHX added right before imaging), and release (2 days of treatment with 0.1 µg/ml CHX before imaging followed by CHX removal immediately before imaging). 500 cells were seeded per well for control and pulse conditions. 1000 cells were seeded per well for CHX and release conditions. After seeding, cells were cultured overnight

without CHX in FluoroBrite™ DMEM (Gibco, A1896701) supplemented with 10% fetal bovine serum (Gibco, 10270-106), 2 mM L-glutamine (Gibco, 25030–024), and 1% penicillin/streptomycin (BioConcept, 401F00H). The next day, CHX was applied at 0.1 µg/ml in CHX and release conditions. During the treatment, the medium was changed every 24h. Before imaging, all wells were washed once with medium. Then, medium containing 0.1 µg/ml CHX was added to CHX and pulse conditions. In control and release conditions, medium without CHX was added. Live imaging was performed with Operetta CLS (Perkin Elmer), 20× objectives (Air immersion, Plan Apochromat, NA 0.8), at 37 °C, 5% CO_2, with 15 min intervals for more than 20 h if not specified otherwise. For the sfGFP channel, the following filters were used: Ex: BP 435-460, 460-490, Em: HC 500-550. For the mOrange2 channel, the following filters were used: Ex: BP 490-515, 530-560, Em: HC 570-650.
Experiments with H1 hESCs and CGR8 mESCs were performed similarly, except for the culture conditions that were as described in the previous section.

Live imaging of the MCFT upon MYCi treatment/release

3 days before imaging, NIH/3T3 cells were seeded on a 96-well plate coated with fibronectin (Sigma, F4759) at a density that does not exceed 80% confluency for each well when imaging starts. Four conditions were designed: control (-MYCi), MYCi (2 days treatment with 64 µM MYCi before imaging), pulse (64 µM MYCi added right before imaging), and release (2 days of treatment with 64 µM MYCi before imaging followed by MYCi removal immediately before imaging). 254 cells were seeded per well for control and pulse conditions. 800 cells were seeded per well for MYCi and release conditions. After seeding, cells were cultured overnight without MYCi in FluoroBrite™ DMEM (Gibco, A1896701) supplemented with 10% fetal bovine serum (Gibco, 10270-106), 2 mM L-glutamine (Gibco, 25030–024), and 1% penicillin/streptomycin (BioConcept, 401F00H). The next day, MYCi was applied at 64 µM in MYCi and release conditions. During the treatment, the medium was changed every 24h. Before imaging, all wells were washed once with medium. Then, medium containing 64 µM MYCi was added to MYCi and pulse conditions. In control and release conditions, medium without MYCi was added. Live imaging was performed with Operetta CLS (Perkin Elmer), 20× objectives (Air immersion, Plan Apochromat, NA 0.8), at 37 °C, 5% CO_2, with 15 min intervals for more than 20 h if not specified otherwise. For the sfGFP channel, the following filters were used: Ex: BP 435-460, 460-490, Em: HC 500-550. For the mOrange2 channel, the following filters were used: Ex: BP 490-515, 530-560, Em: HC 570-650.

SNAP-tag pulse-chase labeling

Cells were seeded and cultured in 96-well plates following the previous “live imaging” method section. 45 minutes before imaging, cells were incubated with an imaging medium that

contained 40 - 80 nM SNAP Cell 647 Sir dye (NEB, S9102S) for 30 min at 37°C, 5% CO_2. Cells were then gently washed five times with fresh medium. The medium was then replaced with a fresh imaging medium containing 1 µM SNAP Cell Block (NEB, S9106S) to prevent the binding of residual SNAP dye to newly synthesized SNAP-tagged proteins. Imaging was performed with an Operetta CLS (Perkin Elmer) microscope, 20× objectives (Air immersion, Plan Apochromat, NA 0.8), at 37 °C 5% CO_2, at 15 min intervals. For the sfGFP channel, the following filters were used: Ex: BP 435-460, 460-490, Em: HC 500-550. For the SNAP channel, the following filters were used: Ex: BP 615-645, BP 650-675, Em: HC 655-760.

Dox pulse-chase experiment

Three days before imaging, NIH/3T3 cells were seeded at a density of 200 cells/well on a 96-well plate coated with fibronectin (Sigma, F4759). After seeding, cells were cultured overnight without dox in FluoroBrite™ DMEM (Gibco, A1896701) supplemented with 10% fetal bovine serum (Gibco, 10270-106), 2 mM L-glutamine (Gibco, 25030–024), and 1% penicillin/streptomycin (BioConcept, 401F00H). The next day, dox (Sigma-Aldrich, D9891) treatments were applied at the desired concentrations. During the treatment, the medium was changed every 24 hours. Before imaging, all wells were washed three times with warm PBS followed by the addition of medium containing the desired dox concentration. Live imaging was performed immediately thereafter (~15min delay) with an Operetta CLS (Perkin Elmer), 20× objectives (Air immersion, Plan Apochromat, NA 0.8), at 37 °C, 5% CO_2, with 15 min intervals for at least 20 h if not specified otherwise. For the sfGFP channel, the following filters were used: Ex: BP 435-460, 460-490, Em: HC 500-550. For the mOrange2 channel, the following filters were used: Ex: BP 490-515, 530-560, Em: HC 570-650.

Imbalance computation

The imbalance θ, introduced in (Martin and Suter 2023) is defined as:

$$\theta(t) = \frac{k(t) \times P(t)}{s(t)}$$

The protein synthesis and decay rates at time *t*, *s(t)*, and *k(t)* respectively, were inferred using the Hierarchical Bayesian inference algorithm introduced hereafter (see also Supplementary Text for details). The total protein level at time *t*, *P(t)*, was calculated by summing up the measured green *G* signal and the inferred black-green B_G signal such that:

$$P(t) = G_{measured}(t) + B_{G,infered}(t)$$

N-Hydroxysuccinimide (NHS ester) labeling and imaging

Cells were seeded in a 96-well plate coated with fibronectin (Sigma, F4759) and cultured overnight. The cell seeding number was adjusted so that none of the wells would be more than 80% confluent on day 7. On day 2, 48 different CHX concentrations ranging from 0.002 to 0.25 µg/mL were applied to cells for the next 6 days. The medium was changed every 48 hours. On day 7, cells were fixed with 4% formaldehyde in PBS for 15 min at RT before washing once with PBS. Then, cells were permeabilized with 100% pre-cooled methanol at -20°C for 10 min. Before staining, cells were washed once with 0.2 M sodium bicarbonate. N-Hydroxysuccinimide (Invitrogen, A37573) was diluted in 0.2 M sodium bicarbonate to a final concentration of 50 µg/mL and applied to cells at RT for 30 min. Cells were washed twice with PBS and mounted with Vectashield containing DAPI (Vector, H-1500-10). Imaging was performed with an Operetta CLS (Perkin Elmer) microscope, 20× objectives (Air immersion, Plan Apochromat, NA 0.8), at RT, using the following filters: Ex: BP 615-645, BP 650-675, Em: HC 655-760 for the NHS-ester channel.

Mass Spectrometry experiments

Sample preparation for Mass Spectrometry

Mass spectrometry-based proteomics-related experiments were performed by the Proteomics Core Facility at EPFL. Each sample was digested by filter aided sample preparation (FASP) (Wiśniewski et al. 2009) with minor modifications. Proteins (20 µg) were reduced with 10 mM TCEP in 8M Urea, 0.1M Tris-HCl pH 8.0 at 37°C for 1 h, and further alkylated in 40mM iodoacetamide at 37°C for 45 min in the dark. Proteins were digested overnight at 37°C using 1/50 w/w enzyme-to-protein ratio of mass spectrometry grade trypsin gold and LysC. Generated peptides were desalted in StageTips using 6 disks from an Empore C18 (3 M) filter based on the standard protocol (Rappsilber, Mann, and Ishihama 2007). Purified peptides were dried down by vacuum centrifugation.

Mass spectrometry

Samples were resuspended in 2% acetonitrile (Biosolve), 0.1% FA and nano-flow separations were performed on a Dionex Ultimate 3000 RSLC nano UPLC system (Thermo Fischer Scientific) on-line connected with an Exploris Orbitrap 480 Mass Spectrometer (Thermo Fischer Scientific). A capillary precolumn (Acclaim Pepmap C18, 3 µm-100Å, 2 cm x 75µm ID) was used for sample trapping and cleaning. A 50 cm long capillary column (75 µm ID; in-house packed using ReproSil-Pur C18-AQ 1.9 µm silica beads; Dr. Maisch) was then used for analytical separations at 250 nl/min over 150 min biphasic gradients. Acquisitions were performed through Top Speed Data-Dependent acquisition mode using a cycle time of 2 seconds. First MS scans were acquired with a resolution of 60’000 (at 200 m/z) and the most intense parent ions were

selected and fragmented by High energy Collision Dissociation (HCD) with a Normalized Collision Energy (NCE) of 30% using an isolation window of 2 m/z. Fragmented ions were acquired with a resolution 15'000 (at 200m/z) and selected ions were then excluded for the following 20 s.

Data analysis

Raw data were processed using MaxQuant 1.6.10.43 (Cox and Mann 2008) against 55286 entries (LR2022_05), Carbamidomethylation was set as fixed modification, whereas oxidation (M), phosphorylation (S, T, Y), acetylation (Protein N-term) and glutamine to pyroglutamate were considered as variable modifications. A maximum of two missed cleavages were allowed and "Match between runs" option was enabled. A minimum of 2 peptides was required for protein identification and the false discovery rate (FDR) cutoff was set to 0.01 for both peptides and proteins. Label-free quantification and normalization was performed by Maxquant using the MaxLFQ algorithm, with the standard settings (Cox et al. 2014).

Statistical analysis was performed using Perseus version 1.6.12.0 (Tyanova et al. 2016) from the MaxQuant tool suite. Reverse proteins, potential contaminants, and proteins only identified by sites were filtered out. Protein groups containing at least 3 valid values in at least one condition were conserved for further analysis. Empty values were imputed with random numbers from a normal distribution (Width: 0.4 and Down shift: 1.8 sd). A two-sample t-test with permutation-based FDR statistics (250 permutations, FDR = 0.01, S0 = 0.5) was performed to determine significant differentially abundant candidates.

Image pre-processing

For background correction, image intensity was modeled the following way:

$$I_{total} = f \times (I_{FOI} + I_{AF} + D)$$

I_{total} is the intensity value of the raw image. f is the uneven illumination pattern. I_{FOI} is the fluorescence signal of interest. I_{AF} is the auto-fluorescence from the medium. D is the dark field signal. D was ignored as it was negligible compared to I_{FOI} or I_{AF}. f was generated by imaging a well with medium only using the same exposure settings. This image was subsequently normalized to its mean pixel intensity. Raw images were divided by the image from the well with medium only to generate flat-field corrected images. I_{AF} was calculated for every single frame by applying the appropriate thresholding method to the field-corrected images, which created a binary image that masked foreground signals I_{FOI}. The threshold was determined using the fifth percentile of the intensity distribution of the pixels belonging to segmented cells. The mask was then enlarged by erosion. Finally, the mean or the peak of pixel intensities was measured from

the unmasked region. We did not generate background-subtracted images but rather subtracted this value from final single-cell measurements inside a Jupyter notebook.

Cell segmentation and tracking

For segmentation and tracking nuclear fluorescent signals, Trackmate (7.1) (Ershov et al. 2022) was used through a groovy script (written by Olivier Burri and Romain Guiet, EPFL) that enables image processing in batch. This script was tailored for using Stardist (Weigert et al. 2020) as the detector to segment cell nuclei on the sfGFP channel. Tracking was then performed with the LAP algorithm (Munkres 1957) within the same script. The script generated Trackmate XML files that allow to review the tracking result with the Trackmate user interface. Both sfGFP and mOrange2 traces were smoothed with a Savitzky-Golay filter (window length: 100, polynomial order: 6) (Savitzky and Golay 1964) before superstatistical modeling. For the CHX pulse and release experiment in hESCs and mESCs, fluorescence trajectories were detrended using the Control and the +CHX conditions, respectively. For the NHS-ester labeling and mESC/hESC experiments, CellPose in Python (Pachitariu and Stringer 2022) was used to segment the nuclei. The masks were then used to retrieve NHS-ester SiR-647 nm integrated intensities of individual cells. All microscopy figure panels and supplementary videos were made using the microfilm package (Witz [2021] 2024) in Python.

Quantification of *k* and k_{deg} from SNAP pulse-chase labeling

To measure k_{deg} with SNAP, the integrated intensity for each single cell trajectory or single lineage (mother and computationally fused daughter cells) trajectory was transformed by natural logarithm, then linear-fitted a robust RANSAC (Fischler and Bolles 1981) regression (random state: 42) from the scikit-learn package 1.0.2 (Pedregosa et al. 2011). Fluorescence intensities of daughter cells resulting from cell division were summed. To measure the total protein decay rate *k* with SNAP (k_{deg} + k_{dil}), the mean intensities for each lineage were transformed by natural logarithm and then linear-fitted with a robust regressor RANSAC (random state: 42). Fluorescence intensities of daughter cells resulting from cell division were averaged.

Quantification of *S* and *k* from the MCFT

The decay rate *k* was computed using the formula derived in the Supplementary Text. The procedure to calibrate the MCFT is given in the Supplementary Text. To compute the rates s, we assumed equilibrium for all our measurements. With μ_G, μ_R, the integrated intensity for sfGFP and mOrange2 fluorescence, and m_G the maturation rate of sfGFP (Fig.1a), we computed the synthesis rate as:

$$s = \mu_G \times \frac{k(m_G + k)}{m_G}$$

s is thus given here in relative units (fluorescence/hour). In the main text, we use *S* when *s* is normalized to the control condition, such that for control conditions we have *S=1*. See Supplementary Text for details. To compute $s_{conc.}$ we used the same equation, replacing the integrated intensity μ_G with the mean intensity $\widehat{\mu_G}$ (average fluorescence intensity per pixel). The equation linking the two observables is:

$$\widehat{\mu_G} = \frac{\mu_G}{\#pixels}$$

In the main text, we use $S_{conc.}$ when $s_{conc.}$ is normalized to the median synthesis rate in a cell line (Fig.6).

Quantification of k_{dil} from time-lapse movies

To measure the k_{dil} we counted cell numbers per imaging frame over time. The dilution rate was then calculated by log2 transformation of the cell number and linear fitting with the RANSAC regressor (random state: 42).

Modeling and inference from MCFT traces

We adopted a superstatistical Bayesian inference algorithm (Mark et al. 2018; Metzner et al. 2015; Mark, Metzner, and Fabry 2014), designed for autoregressive models (AR-1), and applied it to our ordinary differential equation (ODE) systems. Briefly, we computed the (joint) posterior distribution of S and k along with the latent variable B_G at each timepoint and propagated this posterior forward and backward along the MCFT trajectories. In our case, the trajectories used for the inference are G (sfGFP) and R (mOrange2) fluorescence trajectories acquired by live-cell imaging. Propagation of the posterior distribution relies on two hyperparameters chosen for their ability to recapitulate the data (data retrodiction) and fixed for a whole dataset. Details are given in the Supplementary text.

Log-likelihood and bootstrapping for model selection

Log-likelihood was computed using a Gaussian error model. The pseudo-(log) likelihood was used for the actual computation, finally reducing to the residual sum of squares. Briefly, data were compared to the model predictions for the passive adaptation, no-adaptation, and perfect adaptation models. To compute statistics for the log-likelihood estimator, bootstrapping was performed with N=1000 resampling, keeping the sample size constant.

Statistical analysis

Statistical analysis was performed using Python and the scipy.stats package. All details about statistical tests and sample size are available in the figures' legends. $p<0.05$ was considered statistically significant. When Pearson correlation was performed, the statistics (p-value and determination coefficient r^2) were computed and displayed on the figure, or specified in the figure legend. Data binning was performed using an in-house algorithm. Briefly, the number of bins was fixed over the full range of values of the x-axis. For each bin, we then computed the median of the y-values of all data points belonging to it.

Supplementary Text

See related pdf file.

Supplementary Tables

See related Excel files.

Supplementary Movies

See related mp4 files.

References

Alber, Andrea Brigitta, Eric Raphael Paquet, Martina Biserni, Felix Naef, and David Michael Suter. 2018. “Single Live Cell Monitoring of Protein Turnover Reveals Intercellular Variability and Cell-Cycle Dependence of Degradation Rates.” *Mol Cell* 71 (6): 1079-1091.e9. https://doi.org/10.1016/j.molcel.2018.07.023.

Alber, Andrea Brigitta, and David Michael Suter. 2018. “Single-Cell Quantification of Protein Degradation Rates by Time-Lapse Fluorescence Microscopy in Adherent Cell Culture.” *JoVE (Journal of Visualized Experiments)*, no. 132 (February), e56604. https://doi.org/10.3791/56604.

Arimoto, Kyoko, Hiroyuki Fukuda, Shinobu Imajoh-Ohmi, Haruo Saito, and Mutsuhiro Takekawa. 2008. “Formation of Stress Granules Inhibits Apoptosis by Suppressing Stress-Responsive MAPK Pathways.” *Nature Cell Biology* 10 (11): 1324–32. https://doi.org/10.1038/ncb1791.

Balakrishnan, Rohan, Matteo Mori, Igor Segota, Zhongge Zhang, Ruedi Aebersold, Christina Ludwig, and Terence Hwa. 2022. “Principles of Gene Regulation Quantitatively Connect DNA to RNA and Proteins in Bacteria.” *Science* 378 (6624): eabk2066. https://doi.org/10.1126/science.abk2066.

Barry, Joseph D., Donà Erika, Darren Gilmour, and Wolfgang Huber. 2016. “TimerQuant: A Modelling Approach to Tandem Fluorescent Timer Design and Data Interpretation for Measuring Protein Turnover in Embryos.” *Development* 143 (1): 174–79. https://doi.org/10.1242/dev.125971.

Basier, Clovis, and Paul Nurse. 2024. “TOR Regulates Variability of Protein Synthesis Rates.” *The EMBO Journal* 43 (8): 1618–33. https://doi.org/10.1038/s44318-024-00075-8.

Bodor, Dani L., Mariluz Gómez Rodríguez, Nuno Moreno, and Lars E. T. Jansen. 2012. “Analysis of Protein Turnover by Quantitative SNAP-Based Pulse-Chase Imaging.” *Current Protocols in Cell Biology* Chapter 8 (June):Unit8.8. https://doi.org/10.1002/0471143030.cb0808s55.

Cerbini, Trevor, Ray Funahashi, Yongquan Luo, Chengyu Liu, Kyeyoon Park, Mahendra Rao, Nasir Malik, and Jizhong Zou. 2015. “Transcription Activator-like Effector Nuclease (TALEN)-Mediated CLYBL Targeting Enables Enhanced Transgene Expression and One-Step Generation of Dual Reporter Human Induced Pluripotent Stem Cell (iPSC) and Neural Stem Cell (NSC) Lines.” *PloS One* 10 (1): e0116032. https://doi.org/10.1371/journal.pone.0116032.

Cox, Jürgen, Marco Y. Hein, Christian A. Luber, Igor Paron, Nagarjuna Nagaraj, and Matthias Mann. 2014. “Accurate Proteome-Wide Label-Free Quantification by Delayed Normalization and Maximal Peptide Ratio Extraction, Termed MaxLFQ.” *Molecular & Cellular Proteomics: MCP* 13 (9): 2513–26. https://doi.org/10.1074/mcp.M113.031591.

Cox, Jürgen, and Matthias Mann. 2008. “MaxQuant Enables High Peptide Identification Rates, Individualized p.p.b.-Range Mass Accuracies and Proteome-Wide Protein Quantification.” *Nature Biotechnology* 26 (12): 1367–72. https://doi.org/10.1038/nbt.1511.

Cuervo, A. M., A. Palmer, A. J. Rivett, and E. Knecht. 1995. “Degradation of Proteasomes by Lysosomes in Rat Liver.” *European Journal of Biochemistry* 227 (3): 792–800. https://doi.org/10.1111/j.1432-1033.1995.tb20203.x.

Dai, Chun-Ling, Jianhua Shi, Yanxing Chen, Khalid Iqbal, Fei Liu, and Cheng-Xin Gong. 2013. “Inhibition of Protein Synthesis Alters Protein Degradation through Activation of Protein Kinase B (AKT).” *The Journal of Biological Chemistry* 288 (33): 23875–83. https://doi.org/10.1074/jbc.M112.445148.

Deluz, Cédric, Elias T. Friman, Daniel Strebinger, Alexander Benke, Mahé Raccaud, Andrea Callegari, Marion Leleu, Suliana Manley, and David M. Suter. 2016. “A Role for Mitotic Bookmarking of SOX2 in Pluripotency and Differentiation.” *Genes Dev.* 30 (22): 2538–50. https://doi.org/10.1101/gad.289256.116.

Dikic, Ivan, and Zvulun Elazar. 2018. “Mechanism and Medical Implications of Mammalian Autophagy.” *Nature Reviews Molecular Cell Biology* 19 (6): 349–64. https://doi.org/10.1038/s41580-018-0003-4.

Ershov, Dmitry, Minh-Son Phan, Joanna W. Pylvänäinen, Stéphane U. Rigaud, Laure Le Blanc, Arthur Charles-Orszag, James R. W. Conway, et al. 2022. “TrackMate 7: Integrating State-of-the-Art Segmentation Algorithms into Tracking Pipelines.” *Nature Methods* 19 (7): 829–32. https://doi.org/10.1038/s41592-022-01507-1.

Fischler, Martin A., and Robert C. Bolles. 1981. “Random Sample Consensus: A Paradigm for Model Fitting with Applications to Image Analysis and Automated Cartography.” *Communications of the ACM* 24 (6): 381–95. https://doi.org/10.1145/358669.358692.

Honda, Tomoya, Jonas Cremer, Leonardo Mancini, Zhongge Zhang, Teuta Pilizota, and Terence Hwa. 2022. “Coordination of Gene Expression with Cell Size Enables Escherichia Coli to Efficiently

Maintain Motility across Conditions." *Proceedings of the National Academy of Sciences* 119 (37): e2110342119. https://doi.org/10.1073/pnas.2110342119.
Huang, Ming-Jer, Yuan-chih Cheng, Chien-Ru Liu, Shufan Lin, and H. Eugene Liu. 2006. "A Small-Molecule c-Myc Inhibitor, 10058-F4, Induces Cell-Cycle Arrest, Apoptosis, and Myeloid Differentiation of Human Acute Myeloid Leukemia." *Experimental Hematology* 34 (11): 1480–89. https://doi.org/10.1016/j.exphem.2006.06.019.
Jha, Rajiv Kumar, Fedor Kouzine, and David Levens. 2023. "MYC Function and Regulation in Physiological Perspective." *Frontiers in Cell and Developmental Biology* 11:1268275. https://doi.org/10.3389/fcell.2023.1268275.
Kasparek, Petr, Michaela Krausova, Radka Haneckova, Vitezslav Kriz, Olga Zbodakova, Vladimir Korinek, and Radislav Sedlacek. 2014. "Efficient Gene Targeting of the Rosa26 Locus in Mouse Zygotes Using TALE Nucleases." *FEBS Letters* 588 (21): 3982–88. https://doi.org/10.1016/j.febslet.2014.09.014.
Khan, S., M. van den Broek, K. Schwarz, R. de Giuli, P. A. Diener, and M. Groettrup. 2001. "Immunoproteasomes Largely Replace Constitutive Proteasomes during an Antiviral and Antibacterial Immune Response in the Liver." *Journal of Immunology (Baltimore, Md.: 1950)* 167 (12): 6859–68. https://doi.org/10.4049/jimmunol.167.12.6859.
Khmelinskii, Anton, Philipp J. Keller, Anna Bartosik, Matthias Meurer, Joseph D. Barry, Balca R. Mardin, Andreas Kaufmann, et al. 2012. "Tandem Fluorescent Protein Timers for in Vivo Analysis of Protein Dynamics." *Nature Biotechnology* 30 (7): 708–14. https://doi.org/10.1038/nbt.2281.
Klein, Matthew E., Pablo E. Castillo, and Bryen A. Jordan. 2015. "Coordination between Translation and Degradation Regulates Inducibility of mGluR-LTD." *Cell Reports* 10 (9): 1459–66. https://doi.org/10.1016/j.celrep.2015.02.020.
Kristensen, Anders R., Joerg Gsponer, and Leonard J. Foster. 2013. "Protein Synthesis Rate Is the Predominant Regulator of Protein Expression during Differentiation." *Molecular Systems Biology* 9 (1): 689. https://doi.org/10.1038/msb.2013.47.
Liu, Shixuan, Ceryl Tan, Chloe Melo-Gavin, Kevin G. Mark, Miriam B. Ginzberg, Ron Blutrich, Nish Patel, Michael Rape, and Ran Kafri. 2021. "Large Cells Activate Global Protein Degradation to Maintain Cell Size Homeostasis." bioRxiv. https://doi.org/10.1101/2021.11.09.467936.
Mark, Christoph, Claus Metzner, and Ben Fabry. 2014. "Bayesian Inference of Time Varying Parameters in Autoregressive Processes." arXiv. https://doi.org/10.48550/arXiv.1405.1668.
Mark, Christoph, Claus Metzner, Lena Lautscham, Pamela L. Strissel, Reiner Strick, and Ben Fabry. 2018. "Bayesian Model Selection for Complex Dynamic Systems." *Nature Communications* 9 (1): 1803. https://doi.org/10.1038/s41467-018-04241-5.
Martin, Benjamin, and David M. Suter. 2023. "An Out-of-Equilibrium Definition of Protein Turnover." *BioEssays* 45 (6): 2200209. https://doi.org/10.1002/bies.202200209.
Metzner, Claus, Christoph Mark, Julian Steinwachs, Lena Lautscham, Franz Stadler, and Ben Fabry. 2015. "Superstatistical Analysis and Modelling of Heterogeneous Random Walks." *Nature Communications* 6 (June):7516. https://doi.org/10.1038/ncomms8516.
Munkres, James. 1957. "Algorithms for the Assignment and Transportation Problems." *Journal of the Society for Industrial and Applied Mathematics* 5 (1): 32–38.
Nandi, D., E. Woodward, D. B. Ginsburg, and J. J. Monaco. 1997. "Intermediates in the Formation of Mouse 20S Proteasomes: Implications for the Assembly of Precursor Beta Subunits." *The EMBO Journal* 16 (17): 5363–75. https://doi.org/10.1093/emboj/16.17.5363.
Neurohr, Gabriel E., Rachel L. Terry, Jette Lengefeld, Megan Bonney, Gregory P. Brittingham, Fabien Moretto, Teemu P. Miettinen, et al. 2019. "Excessive Cell Growth Causes Cytoplasm Dilution And Contributes to Senescence." *Cell* 176 (5): 1083-1097.e18. https://doi.org/10.1016/j.cell.2019.01.018.
Okuda, A., and G. Kimura. 1988. "Non-Specific Elongation of Cell Cycle Phases by Cycloheximide in Rat 3Y1 Cells, and Specific Reduction of G1 Phase Elongation by Simian Virus 40 Large T Antigen." *Journal of Cell Science* 91 (Pt 2) (October):295–302. https://doi.org/10.1242/jcs.91.2.295.
Pachitariu, Marius, and Carsen Stringer. 2022. "Cellpose 2.0: How to Train Your Own Model." *Nature Methods* 19 (12): 1634–41. https://doi.org/10.1038/s41592-022-01663-4.
Padgett, Joe, and Silvia D. M. Santos. 2020. "From Clocks to Dominoes: Lessons on Cell Cycle Remodelling from Embryonic Stem Cells." *FEBS Letters*, June. https://doi.org/10.1002/1873-3468.13862.
Pakos-Zebrucka, Karolina, Izabela Koryga, Katarzyna Mnich, Mila Ljujic, Afshin Samali, and Adrienne M Gorman. 2016. "The Integrated Stress Response." *EMBO Reports* 17 (10): 1374–95. https://doi.org/10.15252/embr.201642195.

Pedregosa, Fabian, Gaël Varoquaux, Alexandre Gramfort, Vincent Michel, Bertrand Thirion, Olivier Grisel, Mathieu Blondel, et al. 2011. “Scikit-Learn: Machine Learning in Python.” *Journal of Machine Learning Research* 12 (85): 2825–30.

Perez-Pinera, Pablo, David G. Ousterout, Matthew T. Brown, and Charles A. Gersbach. 2012. “Gene Targeting to the ROSA26 Locus Directed by Engineered Zinc Finger Nucleases.” *Nucleic Acids Res* 40 (8): 3741–52. https://doi.org/10.1093/nar/gkr1214.

Ramachandran, Kapil V., Jack M. Fu, Thomas B. Schaffer, Chan Hyun Na, Michael Delannoy, and Seth S. Margolis. 2018. “Activity-Dependent Degradation of the Nascentome by the Neuronal Membrane Proteasome.” *Molecular Cell* 71 (1): 169-177.e6. https://doi.org/10.1016/j.molcel.2018.06.013.

Rappsilber, Juri, Matthias Mann, and Yasushi Ishihama. 2007. “Protocol for Micro-Purification, Enrichment, Pre-Fractionation and Storage of Peptides for Proteomics Using StageTips.” *Nature Protocols* 2 (8): 1896–1906. https://doi.org/10.1038/nprot.2007.261.

Rechsteiner, M., and S. W. Rogers. 1996. “PEST Sequences and Regulation by Proteolysis.” *Trends in Biochemical Sciences* 21 (7): 267–71.

Savitzky, Abraham., and M. J. E. Golay. 1964. “Smoothing and Differentiation of Data by Simplified Least Squares Procedures.” *Analytical Chemistry* 36 (8): 1627–39. https://doi.org/10.1021/ac60214a047.

Schwanhäusser, Björn, Dorothea Busse, Na Li, Gunnar Dittmar, Johannes Schuchhardt, Jana Wolf, Wei Chen, and Matthias Selbach. 2011. “Global Quantification of Mammalian Gene Expression Control.” *Nature* 473 (7347): 337–42. https://doi.org/10.1038/nature10098.

Seinkmane, Estere, Sew Y. Peak-Chew, Aiwei Zeng, Nina M. Rzechorzek, Andrew D. Beale, David CS Wong, and John S. O’Neill. 2022. “Circadian Regulation of Protein Turnover and Proteome Renewal.” bioRxiv. https://doi.org/10.1101/2022.09.30.509905.

Suter, David M., Laetitia Cartier, Esther Bettiol, Diderik Tirefort, Marisa E. Jaconi, Michel Dubois-Dauphin, and Karl-Heinz Krause. 2006. “Rapid Generation of Stable Transgenic Embryonic Stem Cell Lines Using Modular Lentivectors.” *Stem Cells (Dayton, Ohio)* 24 (3): 615–23. https://doi.org/10.1634/stemcells.2005-0226.

Tanaka, K., and A. Ichihara. 1989. “Half-Life of Proteasomes (Multiprotease Complexes) in Rat Liver.” *Biochemical and Biophysical Research Communications* 159 (3): 1309–15. https://doi.org/10.1016/0006-291x(89)92253-5.

Tyanova, Stefka, Tikira Temu, Pavel Sinitcyn, Arthur Carlson, Marco Y. Hein, Tamar Geiger, Matthias Mann, and Jürgen Cox. 2016. “The Perseus Computational Platform for Comprehensive Analysis of (Prote)Omics Data.” *Nature Methods* 13 (9): 731–40. https://doi.org/10.1038/nmeth.3901.

Weigert, Martin, Uwe Schmidt, Robert Haase, Ko Sugawara, and Gene Myers. 2020. “Star-Convex Polyhedra for 3D Object Detection and Segmentation in Microscopy.” In *2020 IEEE Winter Conference on Applications of Computer Vision (WACV)*, 3655–62. https://doi.org/10.1109/WACV45572.2020.9093435.

Wiśniewski, Jacek R., Alexandre Zougman, Nagarjuna Nagaraj, and Matthias Mann. 2009. “Universal Sample Preparation Method for Proteome Analysis.” *Nature Methods* 6 (5): 359–62. https://doi.org/10.1038/nmeth.1322.

Witz, Guillaume. (2021) 2024. “Guiwitz/Microfilm.” Jupyter Notebook. https://github.com/guiwitz/microfilm.

Zatulovskiy, Evgeny, Shuyuan Zhang, Daniel F. Berenson, Benjamin R. Topacio, and Jan M. Skotheim. 2020. “Cell Growth Dilutes the Cell Cycle Inhibitor Rb to Trigger Cell Division.” *Science (New York, N.Y.)* 369 (6502): 466–71. https://doi.org/10.1126/science.aaz6213.

Zhang, Yinan, Justin Nicholatos, John R. Dreier, Stéphane J. H. Ricoult, Scott B. Widenmaier, Gökhan S. Hotamisligil, David J. Kwiatkowski, and Brendan D. Manning. 2014. “Coordinated Regulation of Protein Synthesis and Degradation by mTORC1.” *Nature* 513 (7518): 440–43. https://doi.org/10.1038/nature13492.

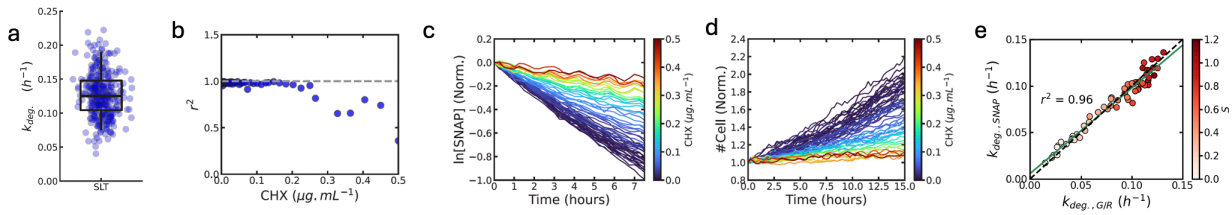

Figure S1: a, Single cell degradation rates k_{deg} of the SLT measured by SNAP pulse-chase labeling. Boxes: interquartile range; horizontal line: median; vertical lines: 5-95 percentiles. N = 324 lineages. **b,** Coefficient of determination r^2 of the fit between cell number trajectories and exponential division model for the different CHX concentrations used. **c,** SNAP pulse-chase labeling after 48 h of treatment with different CHX concentrations. Traces are the normalized (to t = 0 h), log-transformed, sum of the intensities of all segmented nuclei per condition. **d,** Normalized (to t = 0 h) cell number over time after 48 h of CHX treatment. Color scale: CHX concentration for each condition. **e,** k_{deg} computed using SNAP pulse-chase trajectories ($k_{deg,SNAP}$) vs G/R ratios of the MCFT ($k_{deg,G/R}$) for different values of *S*. Values of *S* were normalized to *S* without CHX treatment. x=y black dashed line: perfect concordance between the two ways of computing k_{deg}. Green plain line: best linear fit (r^2 = 0.96) between $k_{deg,SNAP}$ and $k_{deg,G/R}$.

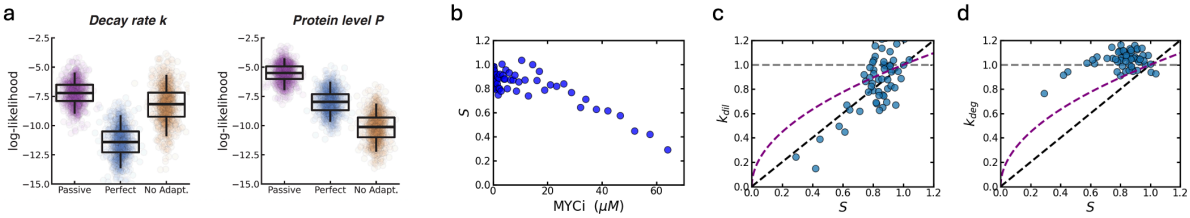

Figure S2: Maximum likelihood confirms passive adaptation as the most likely model in NIH/3T3 cells, and unbinned data for the MYCi experiment. a, Log-likelihood for the different models, using both decay rate *k* and protein level *P* data. **b**, Fold-change in *S* with respect to MYCi concentration (unbinned data). **c,d,** Fold-change in k_{dil} (**c**) and k_{deg} (**d**) versus fold-change in *S* upon MYCi treatment (unbinned data). Black dashed lines: prediction for perfect adaptation; Gray dashed lines: prediction for no adaptation. Purple dashed curved lines: prediction for passive adaptation. The values shown for *S*, k_{deg} and k_{dil} are normalized on the respective values for control conditions.

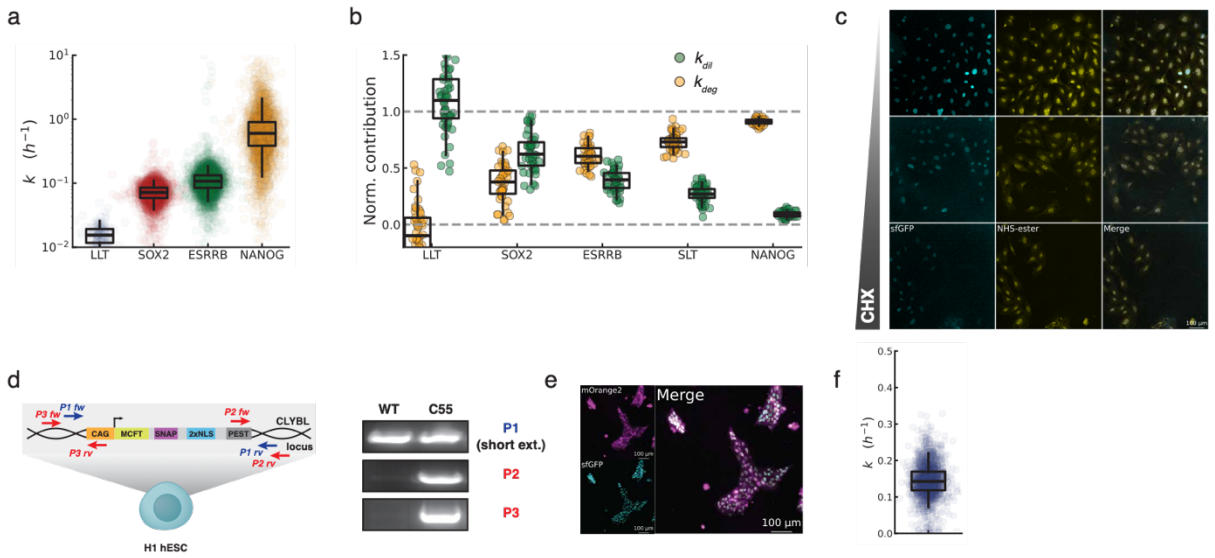

Figure S3: Characterization of NIH/3T3 and hES cell lines. a, Single cell decay rates of the LLT (blue), SOX2 (red), ESRRB (green), and NANOG (orange) proteins. Boxes: interquartile range; horizontal line: median; vertical line: 5-95 percentiles. N = circa 150 (LLT), 3500 cells otherwise. **b,** Normalized contributions of k_{deg} (yellow) and k_{dil} (green) to k for a given S (see Methods)**.** Boxes: interquartile range; horizontal line: median; vertical line: 5-95 percentiles. Horizontal gray dashed lines: minimum (y=0) and maximum (y=1) possible values. **c**, Snapshots in the green (sfGFP - magenta) and NHS-ester channels (yellow) of NIH/3T3 SLT cell populations treated with different CHX concentrations (from top to bottom: 0.008, 0.1125, and 0.5 µg/mL) for 6 days. **d,** Left: Scheme of the MCFT construct knocked into H1 hESCs at the CLYBL locus. Right: PCR genotyping of the knock-in clones. P1, P2, and P3 refer to the set of primers used for PCR. A band in the upper panel indicates the amplification of at least one WT locus. WT: wild-type; C55: selected clone knocked-in into the CLYBL locus with the SLT. **e**, Snapshot of the hESC line harboring the SLT (sfGFP: cyan; mOrange2: magenta). **f,** k of the SLT measured using G/R ratio in the hESC knock-in cell line. Boxes: interquartile range; horizontal line: median; vertical line: 5-95 percentiles. N = 2142 cells.

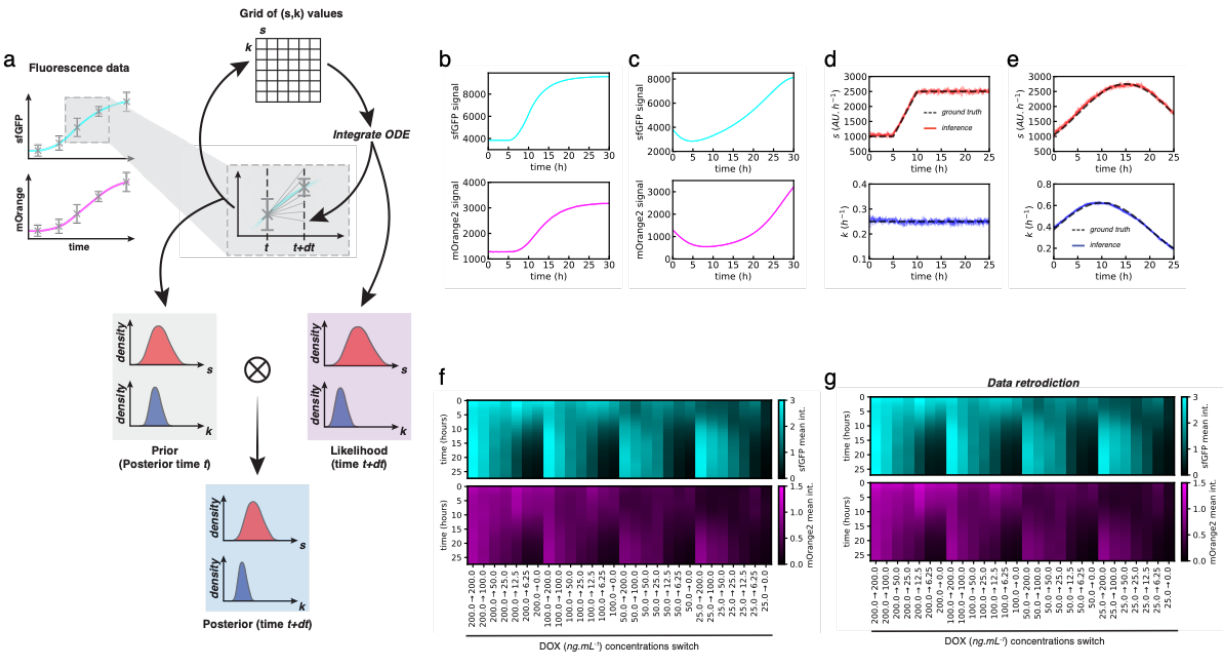

Figure S4: Determining temporal variations in *S* and *k* using a hierarchical superstatistical Bayesian inference algorithm. a, Scheme of the inference strategy. sfGFP (cyan) and mOrange2 (magenta) fluorescence trajectories are both used in the inference. The algorithm iteratively uses each point at time *t* and *t+dt* of the fluorescence trajectory to compute a likelihood for the values of *S* and *k* at time *t*. The convolution of the likelihood distribution with the prior distribution (i.e. the posterior distribution computed at time *t*) allows obtaining the posterior distribution for *S* and *k* for time *t+dt*. This process is then iterated on timepoints *t+dt* and *t+2dt*, etc., for all data points available. **b,** sfGFP (cyan) and mOrange2 (magenta) fluorescence trajectories generated in-silico for a linear increase of *S* between 5 and 10 hours. **c,** sfGFP (cyan) and mOrange2 (magenta) fluorescence trajectories generated in silico for phase-shifted sinusoidal variations of *S* and *k*. **d,** Inferences of the time variation of *S* and *k* from the trajectories in **b. e,** Inferences of the time variation of *S* and *k* from the trajectories in **c. f,** Smoothed sfGFP (cyan) and mOrange2 (magenta) trajectories for experiments with changes in dox concentrations. **g,** Data retrodiction for sfGFP (cyan) and mOrange2 (magenta) fluorescence trajectories.

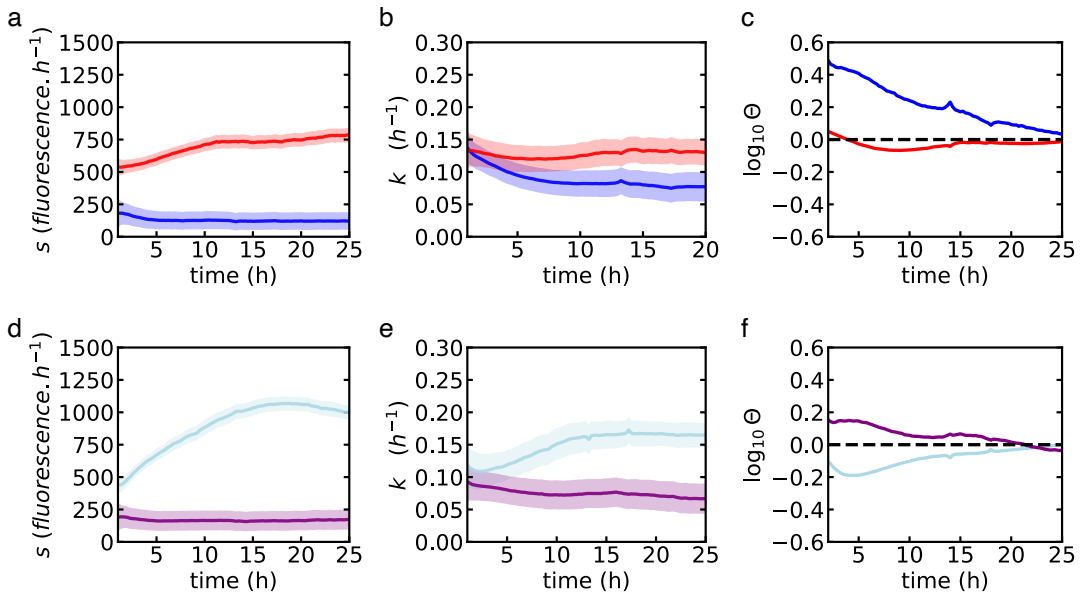

Figure S5: Time-lapse imaging of NIH/3T3 upon pulse/release with MYCi (64 µM). *S* (**a,d**), *k* (**b,e**) and imbalance (**c,f**) trajectories inferred from MCFT measurements during MYCi pulse (**a-c**) or release (**d-f)**. Red: control conditions. Dark blue: MYCi pulse. Purple: continuous MYCi treatment. Light blue: MYCi release. (**a-b**) and (**d-e**), plain lines: average of the posterior distribution; shaded regions: SD of the posterior distribution.

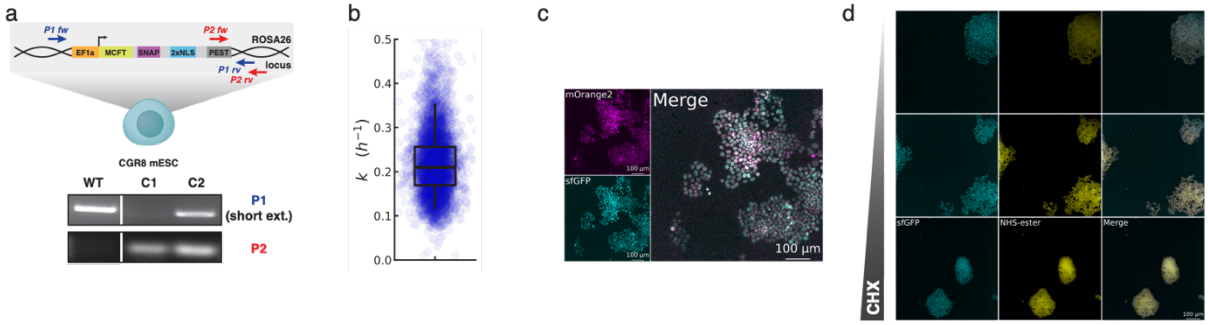

Figure S6: Characterization of the mESC SLT knock-in cell line. a, Scheme of the SLT construct knocked into CGR8 cells at the ROSA26 locus. 2xNLS: two copies of a Nuclear Localization Signal. PCR genotyping of the knock-in clones. P1 and P2 refer to the set of primers used for PCR. A band in the upper panel indicates the amplification of at least one WT locus. WT: wild-type CGR8 mESCs; C1, C2: clones knocked into the ROSA26 locus with the SLT. An irrelevant lane was sliced from the gel picture. C1 was selected for all experiments. **b,** *k* of the SLT measured using G/R ratio in the mESC knock-in cell line. Boxes: interquartile range; horizontal line: median; vertical line: 5-95 percentiles. N = 4790 cells. **c**, Snapshot of green (cyan) and red (magenta) fluorescence of the mESC line harboring the SLT. **d**, Snapshots in the sfGFP (cyan) and NHS-ester (yellow) channels of mESC SLT cell populations treated with different CHX concentrations (from top to bottom: 0.008, 0.1125, and 0.5 µg/mL) for 48 hours.

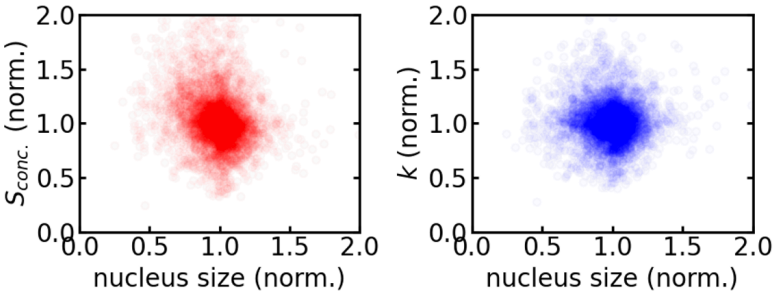

Figure S7: $S_{conc.}$ and k do not correlate with nucleus size.

Supplementary table legends

Supplementary Table 1: CHX concentration used for the steady-state experiment. Concentrations are given in µg/mL, following the layout used to perform the experiment in 96-well plates. The highlighted CHX concentrations are the ones used to show representative microscopy snapshots in the main figures.

Supplementary Table 2: MYCi concentration used for the steady-state experiment. Concentrations are given in µM, following the layout used to perform the experiment in 96-well plates. The highlighted MYCi concentrations are the ones used to show representative microscopy snapshots in the main figures.

Supplementary Table 3: List of primers used for genotyping the cell lines generated in this study.

Supplementary movie legends

Supplementary Movie 1: CHX (0.1 µg/mL) pulse for NIH/3T3 SLT.

Supplementary Movie 2: CHX (0.1 µg/mL) pulse release NIH/3T3 SLT.

Supplementary Movie 3: CHX (0.1 µg/mL) pulse for hESC SLT.

Supplementary Movie 4: CHX (0.1 µg/mL) release for hESC SLT.

Supplementary Movie 5: CHX (0.1 µg/mL) pulse for mESC SLT.

Supplementary Movie 6: CHX (0.1 µg/mL) release for mESC SLT.

For all Supplementary movies, one field of view is shown. One snapshot was taken every 15 minutes in the green and red fluorescence channels. Images are flat field-corrected and background-subtracted (Methods).